Colloids and Surfaces A: Physicochemical and Engineering Aspects 749 (2026) 141158

Contents lists available at ScienceDirect

Colloids and Surfaces A: Physicochemical and Engineering Aspects

journal homepage: www.elsevier.com/locate/colsurfa

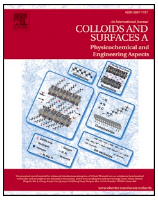

In situ surface nanoengineering of Fe-based amorphous alloy ribbons co-induced by periodate and ultraviolet irradiation for efficient water decontamination

Kunheng Zou [a], Zhenxuan Zhang [a,*], Yujian Li [a], Yu Zhang [a], Mengting Yang [b], Jie Dong [a], Chaoqun Pei [a], Xiong Liang [a,*], Jiang Ma [a,*]

[a] *College of Mechatronics and Control Engineering, Shenzhen University, Shenzhen 518060, China*
[b] *College of Chemistry and Environmental Engineering, Shenzhen University, Shenzhen 518060, China*

HIGHLIGHTS

- *In situ* nanoengineering converted amorphous ribbons into nano-interfaces.
- The synergistic system enabled efficient degradation and mineralization.
- Amorphous ribbons show 21–30 times higher catalytic rates than crystalline or powder forms.
- Singlet oxygen was identified as the dominant reactive species.
- Amorphous ribbons retained 95.8% MO removal efficiency after 8 reuse cycles.

GRAPHICAL ABSTRACT

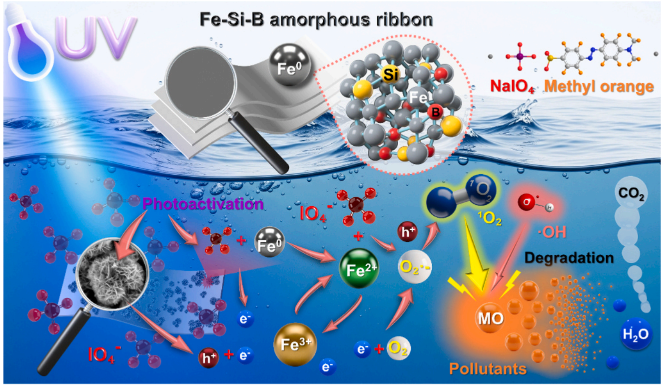

ARTICLE INFO

Keywords:
Fe-Si-B amorphous alloy ribbons (Fe-AR)
Periodate activation
Surface nanoengineering
UV irradiation
Organic pollutant degradation

ABSTRACT

This study reports a UV-enhanced periodate (PI) activation strategy for reaction-driven *in situ* nanoengineering of $Fe_{78}Si_9B_{13}$ amorphous alloy ribbons (Fe-AR) toward efficient methyl orange degradation under near-neutral conditions. The key issue addressed is whether an amorphous alloy surface can undergo self-optimizing dynamic reconstruction in a PI oxidative environment, thereby overcoming the passivation bottleneck of conventional iron-based catalysts. During the Fe-AR/UV/PI reaction, the initially smooth ribbon surface was spontaneously transformed into a three-dimensional nanostructured active interface, accompanied by a wettability transition from hydrophobicity to high hydrophilicity, with the water contact angle decreasing from 88.7° to 12.0°. Under 1 mmol L^{-1} PI and 30 mW cm^{-2} UV irradiation, 98.10% removal of methyl orange (20 mg L^{-1}) was achieved within 50 min, with an apparent rate constant of 0.1378 min^{-1} , which was 21.2 and 30.0 times higher than those of the crystalline ribbon and commercial Fe powder, respectively. Comparative experiments, density functional theory calculations, and electrochemical analyses demonstrated that the enhanced performance was mainly attributed to the intrinsic amorphous structure, stronger PI adsorption, faster interfacial

---

* Corresponding authors.
E-mail addresses: zxzhang@szu.edu.cn (Z. Zhang), xliang@szu.edu.cn (X. Liang), majiang@szu.edu.cn (J. Ma).

https://doi.org/10.1016/j.colsurfa.2026.141158
Received 5 May 2026; Received in revised form 12 June 2026; Accepted 23 June 2026

electron transfer, and continuous generation of reactive surface sites. Mechanistic investigations indicated that singlet oxygen ($^1O_2$) served as the dominant reactive species, while ·OH and O_2·$^-$ acted as auxiliary species. Moreover, 95.8% degradation efficiency was retained after eight cycles, and effective degradation of methylene blue and tetracycline was also achieved. This work demonstrated that amorphous alloy catalysts could be self-activated through oxidative surface reconstruction, providing a promising strategy for developing anti-passivation and high-performance catalytic materials for water purification.

1. Introduction

The continuous accumulation of organic pollutants in aquatic environments, including dyes, antibiotics, and natural organic matter, poses a long-term threat to both ecosystems and human health, thereby creating an urgent demand for more efficient water treatment technologies [1]. In particular, wastewater generated by textile, pharmaceutical, and food-processing industries has become a major environmental concern because of its large discharge volume, complex composition, and potential toxicity. Pollutants such as synthetic dyes and pharmaceutical residues can exert severe adverse effects on aquatic organisms and human health, including carcinogenic, mutagenic, and antibiotic resistance-related risks [2]. In this context, advanced oxidation processes (AOPs) have attracted extensive attention owing to their ability to generate highly reactive oxidative species for the efficient degradation and even complete mineralization of refractory contaminants [3]. Among various AOPs, iron-based Fenton-like processes have been widely studied due to their cost-effectiveness and environmental friendliness [4,5]. Nevertheless, conventional heterogeneous iron-based catalysts such as iron powder and iron oxides often suffer from sluggish Fe^{2+}/Fe^{3+} cycling, high activity only under strongly acidic conditions, and rapid passivation of active sites, all of which severely restrict their practical application [6]. Therefore, the development of new Fenton-like catalysts with high intrinsic activity, excellent durability, and broad pH adaptability remains a central challenge in this field.

To overcome these limitations, increasing attention has been paid toward AOPs alternative oxidants like periodate (PI) [7]. Activated PI systems can involve high-valent iron species, reactive iodine species (RIS), and reactive oxygen species (ROS), thus exhibiting considerable potential for pollutant degradation [8–10]. A range of activation approaches has been explored, including energy-driven methods such as ultraviolet (UV) irradiation [11–13], metal-free homogeneous catalysis [14], and heterogeneous catalysis. Various catalytic materials have been investigated for PI activation, including transition metal oxides such as $CoFe_2O_4$ [15], Fe_2O_3 [16,17]), Cu_2O nanocrystals [18], advanced photocatalysts (e.g. *g*-C_3N_5 [19]) and single-atom catalysts [20]. Despite these advances, the development of a simple, low-cost PI activator that simultaneously delivers ultrahigh catalytic activity and long-term operational stability remains highly desirable.

Fe-based materials have been widely studied for water treatment because of their low cost and high catalytic efficiency. Among emerging Fe-based catalytic materials, Fe-based amorphous alloys, also known as metallic glasses, have attracted growing interest because of their unique atomic configurations and electronic structures [21]. These materials have demonstrated excellent versatility in activating a variety of oxidants, including traditional H_2O_2 [22], persulfates (PDS/PMS) [23], and peracetic acid (PAA) [24], highlighting their broad catalytic potential. Unlike crystalline materials with long-range ordered atomic arrangements, amorphous alloys possess a disordered, liquid-like structure characterized by high free energy, abundant unsaturated active sites [25], and superior interfacial electron-transfer capability, enabling them to outperform their crystalline counterparts in many catalytic reactions [26,27]. However, previous studies have largely treated amorphous alloys as static catalysts, paying insufficient attention to the dynamic evolution of their metastable structures under oxidative conditions and the resulting impact on catalytic performance [28].

Although Fe-based amorphous alloys have shown excellent performance in activating conventional oxidants such as persulfates and H_2O_2, their application in PI activation remains largely unexplored. However, unlike traditional peroxydisulfate systems that rely primarily on sulfate radicals, PI activation features a fundamentally distinct pathway by generating a network of reactive iodine radicals and selectively producing massive amounts of singlet oxygen. These distinct mechanistic features endow the PI system with extraordinary oxidizing power, remarkable resistance to background interference in complex water matrices, and broader environmental adaptability, making the exploration of amorphous alloys for PI activation particularly promising. To address this gap, the present study constructed a synergistic $Fe_{78}Si_9B_{13}$ amorphous alloy ribbons (Fe-AR)/UV/PI system. The central concept is to exploit the metastable nature of the amorphous alloy to trigger an *in situ* self-activation process under oxidative conditions, thereby promoting spontaneous surface reconstruction, catalyst self-optimization, and substantial enhancement of catalytic performance [29]. We hypothesize that the coupled UV/PI environment can not only activate PI efficiently, but also dynamically reconstruct the surface of Fe-AR, generating a highly active nanostructured interface that further promotes catalytic oxidation. Accordingly, this study aims to: (1) evaluate the degradation efficiency of the Fe-AR/UV/PI system toward representative organic pollutants, including methyl orange, methylene blue, and tetracycline; (2) elucidate the *in situ* self-activation mechanism through multidimensional characterization of surface nanoengineering, wettability evolution, and valence-state reconstruction; (3) reveal the fundamental origins of the catalytic superiority of the amorphous structure by combining theoretical calculations with electrochemical analysis; and (4) identify the dominant reactive species, clarify the catalytic pathways, and assess the long-term operational stability of the system. Methyl orange was selected as the primary model pollutant because of its widespread occurrence in textile wastewater, high toxicity, and resistance to conventional treatment methods [30], making it a suitable probe for evaluating the performance of novel catalytic systems. Methylene blue and tetracycline were further employed to verify the versatility and robustness of the catalytic system. Overall, this work not only develops an efficient strategy for water purification, but also provides new insights into the design of self-optimizing catalytic materials capable of autonomous surface nanoengineering during operation.

2. Materials and methods

2.1. Materials

Sodium periodate ($NaIO_4$, 99.8%) was purchased from Sigma-Aldrich. Methylene Blue (98%), methyl orange (98%), and tetracycline (99.5%), L-histidine (L-His, 99.5%), *tert*-butanol (TBA, 99.5%), *p*-benzoquinone (*p*-BQ, 99%), phenol (99.5%), sodium hydroxide (NaOH, 97%), 5,5-dimethyl−1-pyrroline-N-oxide (DMPO), 2,2,6,6-tetramethyl−4-piperidone (TEMP, 97%), methyl phenyl sulfoxide (PMSO, 98%), methanol (MeOH, 99.5%), sodium sulfate (Na_2SO_4), and isopropanol (IPA, 99.5%) were purchased from Macklin (Shanghai, China). Sulfuric acid (H_2SO_4, 98%) was obtained from Xilong Chemical (Guangdong, China), while ultrapure water was used as the reaction medium for all catalytic degradation experiments. The preparation process of the $Fe_{78}Si_9B_{13}$ amorphous alloy ribbons using the single-roller melt-spinning technique is illustrated in Fig. 1. The Fe-Si-B crystalline alloy ribbons were prepared by annealing the as-synthesized amorphous ribbons in a vacuum furnace at 873.15 K (600 °C) for 1 h, followed by furnace cooling to room temperature to ensure complete crystallization. Detailed fabrication protocols for the Fe-ARs and Fe-Si-B crystalline alloy (Fe-C) ribbons are provided in Text S1 of the Supporting Information (SI). Commercial Fe powder (99%, 100 mesh) was obtained from Macklin (Shanghai, China).

2.2. Materials characterization

X-ray diffraction (XRD, Rigaku MiniFlex600) with Cu Kα radiation was employed to distinguish the broad diffuse halo of the Fe-AR from the sharp diffraction peaks of the Fe-Si-B crystalline ribbon (Fe-CR) and Fe powder (Fe-P), thereby confirming its amorphous structure. X-ray photoelectron spectroscopy (XPS, Thermo Scientific K-Alpha) was used to probe the surface elemental composition, chemical valence states, and their evolution under different reaction conditions, thereby elucidating their correlation with the catalytic activity of Fe-AR. X-ray absorption fine structure (XAFS) measurements were conducted using a Rapid XAFS 2 M (XAFS Tech) instrument. A field-emission scanning electron microscope (FE-SEM, FEI QUANTA FEG 650) was used to characterize the surface morphology, microstructure, and defect features of the three Fe-based materials. Energy-dispersive X-ray spectroscopy (EDS) further revealed the microscale elemental distribution and clarified the relationship between elemental migration and catalytic behavior. Electrochemical measurements were performed to evaluate the electron-transfer characteristics, kinetics, and underlying mechanisms of the three Fe-based materials during catalysis. Density functional theory (DFT) calculations were conducted to compare the adsorption energies (E_{ads}) of PI on the Fe-Si-B amorphous alloy, Fe-Si-B crystalline alloy, and pure Fe. Detailed computational methods are provided in Text S2 of the SI.

2.3. Experimental setup

The photocatalytic degradation experiments were carried out in cylindrical borosilicate glass reactors with a working volume of 40 mL. The outer surface of each reactor was wrapped with a high-thermal-conductivity silicone pad, and a constant-temperature cooling fan was employed to maintain the reaction temperature at 26 ± 1 °C. The initial concentrations of methyl orange (MO), methylene blue (MB), and tetracycline (TC) were set as 20 mg L^{-1}, 20 mg L^{-1}, and 40 mg L^{-1}, respectively. The dosage of Fe-AR was fixed at 1.0 g L^{-1}. Both of the UV light source and the reactor were placed in a dark box, with the distance between the reactor and the lamp maintained at 5 cm. Irradiation was provided by a UV lamp (LG UV6565, South Korea) with a maximum emission wavelength of 365 nm. The light intensity was measured using a UV power meter (LinShang LS137, China). Before each experiment, the UV lamp was operated for 15 min to ensure a stable light intensity. To evaluate degradation performance under different operating conditions, experiments were conducted with different $NaIO_4$ dosages (1, 2, and 5 mmol L^{-1}) and UV intensities (30, 60, and 90 mW cm^{-2}). The initial pH was adjusted with sodium hydroxide or sulfuric acid solution, and the pH of the reaction system was monitored using a pH meter (STARTER 3100, PerkinElmer). All degradation experiments were performed in triplicate, and the reported results represent the average values.

2.4. Analytical methods

The concentrations of MO, MB, and TC during the catalytic degradation process were determined using a UV–visible spectrophotometer (UVmini−1280, SHIMADZU). Their concentrations were quantified from the corresponding UV–visible absorption spectra using the characteristic absorption wavelengths of 464 nm for MO, 664 nm for MB, and 366 nm for TC, respectively. According to the linear relationship between absorbance and concentration based on the Lambert–Beer law, calibration curves were established to calculate the actual pollutant concentrations (Fig. S1). The degradation kinetics were analyzed using a pseudo-first-order kinetic model:

$$\ln(C_t/C_0) = -kt$$

where C_0 is the initial concentration, C_t is the concentration at reaction time t; k (min^{-1}) is the pseudo-first-order reaction rate constant, and t (min) is the reaction time. In addition, the total organic carbon (TOC) was measured using a TOC analyzer (SHIMADZU TOC-L) to evaluate the mineralization efficiency of the pollutants.

2.5. Electron paramagnetic resonance analysis

Electron paramagnetic resonance (EPR) spectroscopy combined with spin-trapping is a powerful technique for identifying reactive species. EPR measurements were performed using an EPR spectrometer (EPR200M, Chinainstru & Quanttech, China). DMPO and TEMP were used as spin-trapping agents for the detection of short-lived reactive species. For real-time detection of spin adducts, a reaction system containing sodium periodate (PI, 1 mmol L^{-1}) and Fe-AR (1 g L^{-1}) in 20 mL of ultrapure water was irradiated with 365 nm UV light at an intensity of 30 mW cm^{-2} for 5 min. The resulting solution was then rapidly mixed with DMPO (100 mmol L^{-1}) or TEMP (20 mmol L^{-1}) to ensure efficient spin trapping. Subsequently, a small aliquot of the mixture was transferred into a capillary tube, sealed with vacuum grease, and immediately placed in the EPR resonant cavity for analysis. The EPR spectra were

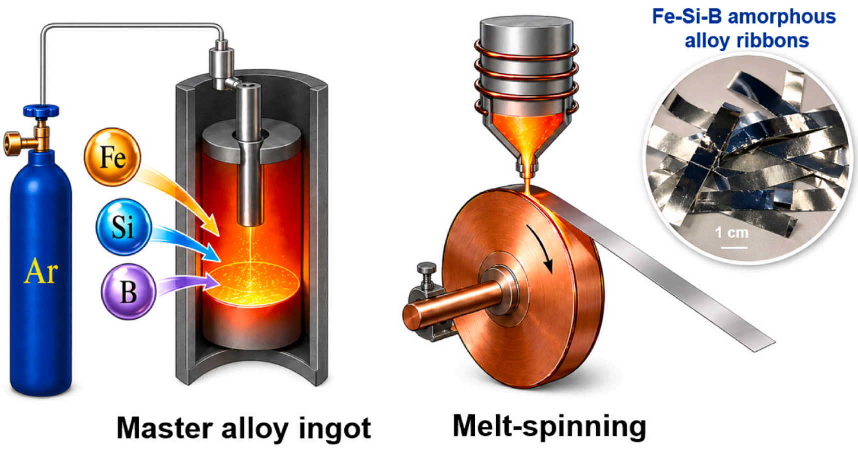

Fig. 1. Preparation of $Fe_{78}Si_9B_{13}$ amorphous alloy ribbons by single-roller melt spinning.

recorded at room temperature under the following operating conditions: center field, 3490.000 G; stabilization delay time, 10 ms; sweep width, 80.000 G; modulation amplitude, 2 G; microwave power, 1 mW; and power attenuation, 20.0 dB.

3. Results and discussion

3.1. *In situ surface nanoengineering of Fe-AR*

To investigate the surface morphological evolution of Fe-AR, SEM was employed to examine the changes induced by PI exposure under UV irradiation. A distinct *in situ* nanoengineering process driven by oxidative etching was observed on the surface of Fe-AR. Previous studies have shown that the catalytic performance of amorphous alloys is closely related to their unique disordered atomic structure and dynamic surface behavior [31,32]. In the synergistic Fe-AR/UV/PI system, the ribbon surface underwent a dynamic transformation from a smooth, hydrophobic state to a three-dimensional hierarchical active interface. During this process, the initially smooth surface was progressively converted into a hydrophilic interface covered with nanoflower-like structures, demonstrating that the UV/PI system can effectively induce the surface reconstruction of the amorphous catalyst.

As shown in Fig. 2a, the pristine Fe-AR exhibited a smooth and flat surface at the microscale, with an initial water contact angle of 88.7°,

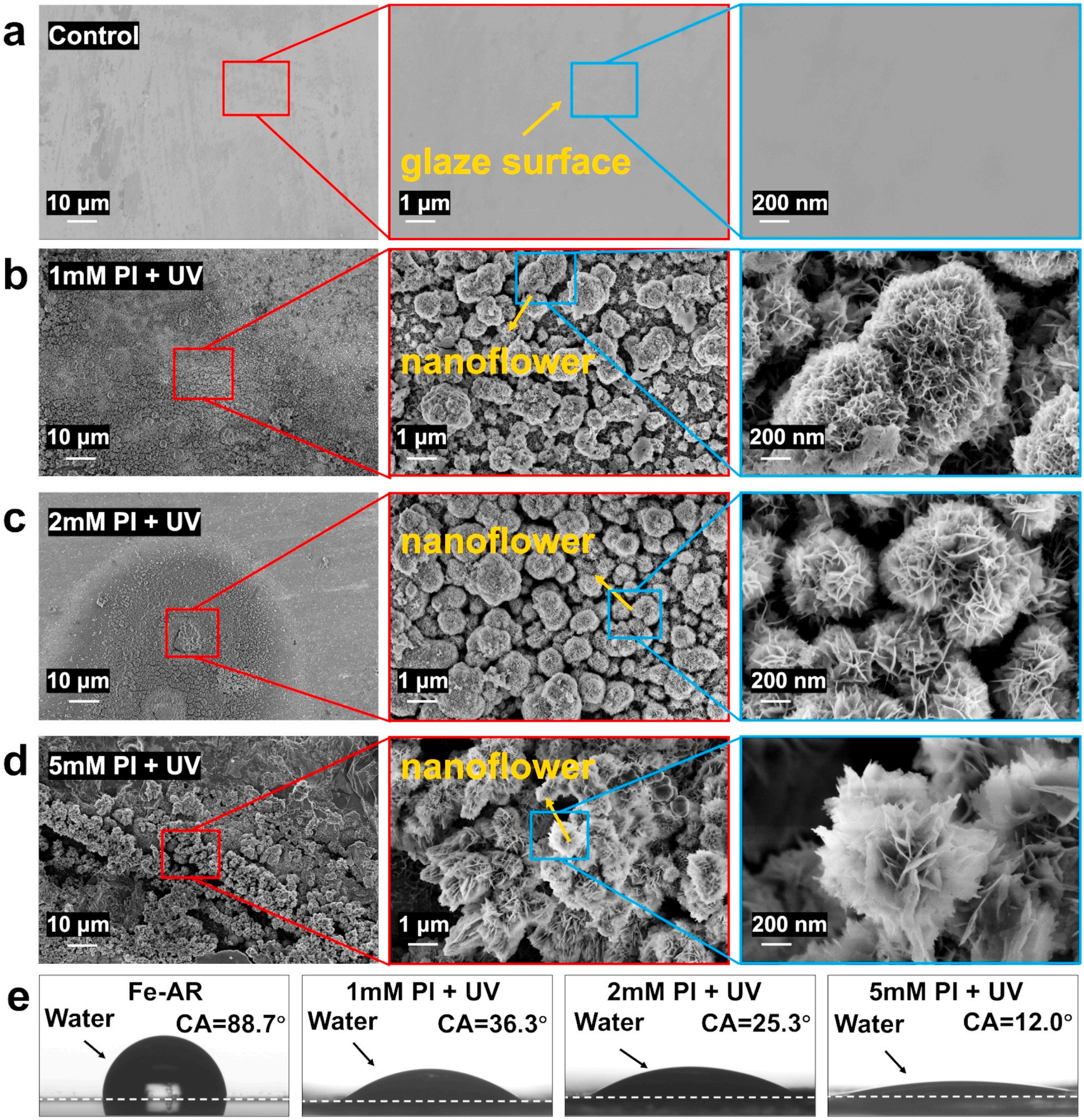

Fig. 2. (a) SEM image of pristine Fe-AR. (b-d) SEM images of Fe-AR exposure to 1, 2, and 5 mmol L^{-1} PI under UV irradiation (30 mW cm^{-2}). (e) Water contact angle of Fe-AR exposure to 1, 2, and 5 mmol L^{-1} PI under UV irradiation (30 mW cm^{-2}).

indicating hydrophobicity (Fig. 2e). However, in the Fe-AR/UV/PI system, this metastable surface is rapidly activated. At the initial stage of the reaction, predominantly driven by the corrosive oxidation of PI, oxidative etching triggered by the reactive species generated in the system serves as the starting point for surface evolution [33]. After treatment with a low PI concentration (1 mmol L^{-1}), the ribbon surface became roughened and very fine nanoflower-like structures emerged (Fig. 2b).

As the reaction proceeded or the PI concentration increases (Fig. 2c and Fig. 2d), the surface evolution became markedly more pronounced. These *in situ* generated nanostructures establish a potential difference relative to the surrounding amorphous matrix, thereby inducing a micro-galvanic effect. Subsequently, this micro-galvanic couple serves as the primary driving force for the accelerated growth of the nanostructures, which is concurrently further promoted by a photoelectrochemical effect induced by UV irradiation on the newly formed semiconducting oxide layer. Driven by these synergistic effects, local corrosion and product deposition are further accelerated, promoting the growth of the nanostructures into micron-scale oxide clusters and the gradual formation of large reaction pits. Under higher PI concentrations,

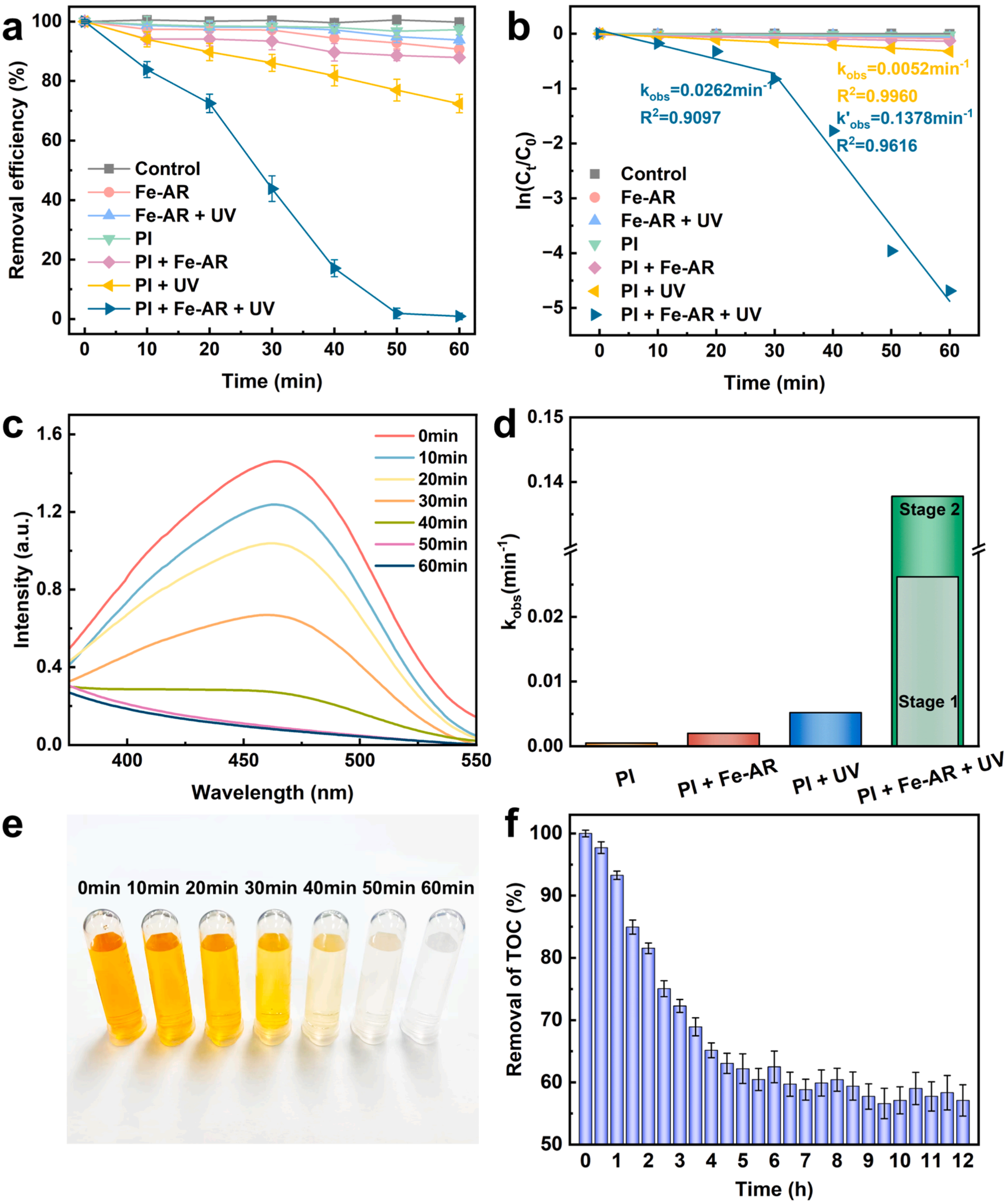

Fig. 3. Degradation performance of the Fe-AR/UV/PI synergistic system towards MO. (a) Degradation process of MO in different systems. (b) Pseudo-first-order kinetic fits of (a). (c) UV absorption spectra changes of MO solution during the degradation process (0–60 min). (d) Comparison of reaction constants for degradation of MO by different treatment groups. (e) Photo of MO solution decolorization over time. (f) Total organic carbon removal efficiency during MO degradation by Fe-AR/UV/PI synergistic system. Experimental conditions: $[MO]_0 = 20$ mg L^{-1}. [Fe-AR] = 1.0 g L^{-1}. [PI] = 1 mmol L^{-1}. UV intensity = 30 mW cm^{-2}.

the continuous growth, rupture, and partial exfoliation of these oxide clusters continuously expose fresh amorphous matrix and generate new active sites. As a result, a complex hierarchical interface composed of extensive nanoflower-like features and deep reaction pits was eventually constructed (Fig. 2d).

This dramatic morphological evolution fundamentally changes the physicochemical properties of the Fe-AR surface. The most prominent change is the substantial enhancement in wettability. As shown in Fig. 2e, the treated Fe-AR surface rapidly transformed from a hydrophobic state (88.7°) to a highly hydrophilic one, where the water droplet spreaded almost completely and the contact angle decreased to as low as 12.0°. This wettability transition can be attributed to two main factors. First, the *in situ* formed nanostructures significantly increase the surface roughness. Second, the newly formed surface layer was possibly composed of hydrophilic iron oxides/oxyhydroxides.

Overall, the surface reconstruction driven by oxidative etching, micro-galvanic coupling, and photo-electrochemical effects transformed the initially inert Fe-AR into a structurally complex active interface. This highly hydrophilic interface, with its enlarged specific surface area, facilitated contact between pollutants and the catalyst, thereby enhancing interfacial mass transfer. More importantly, it could provide abundant reactive sites for efficient PI activation, ensuring the sustained generation of dominant reactive species for pollutant degradation. Therefore, this unique *in situ* dynamic evolution is central to understanding the origin of the catalytic performance of this amorphous alloy-based catalysis degradation system.

3.2. The degradation performance of MO

To systematically evaluate the catalytic performance of the Fe-AR/UV/PI synergistic system and verify the synergy among its components, a series of degradation experiments were conducted on the degradation of azo dye MO [34,35]. As shown in Fig. 3a and b, within 60 min, the single-component systems containing only Fe-AR (1 g L^{-1}) or PI (1 mmol L^{-1}) exhibited negligible MO degradation, indicating that the direct reducing ability of Fe-AR and the intrinsic oxidizing capacity of unactivated PI were both very limited. In comparison, the dual-component systems displayed moderate catalytic activity. The degradation of MO by Fe-AR activated by PI (Fe-AR + PI) achieved a final degradation efficiency of only 12.09%, which may be attributed to the role of Fe-AR as a zero-valent iron source that continuously releases Fe(II) through surface corrosion, thereby activating PI to generate oxidative species. The degradation of MO by PI under UV irradiation (PI + UV) showed a slightly higher degradation rate of 27.61%, which can be ascribed to the photolysis of PI under UV irradiation, producing reactive species such as ·OH and IO_3· [36]. Notably, when Fe-AR, PI, and UV irradiation were combined, the degradation efficiency of MO increased dramatically, reaching 98.10% within 50 min.

From the kinetic perspective (Fig. 3b), the apparent reaction rate constant (k) of the ternary synergistic system in the later stage of the reaction reached 0.1378 min^{-1}, which was 68.9 times and 26.5 times higher than those of the Fe-AR + PI system ($k = 0.0020$ min^{-1}) and the PI + UV system ($k = 0.0052$ min^{-1}). This non-linear enhancement in catalytic activity clearly demonstrated a strong synergistic effect among Fe-AR, PI, and UV irradiation. It's noteworthy that the degradation kinetics of MO exhibited a distinct two-stage behavior. In the initial stage (0–30 min), the apparent rate constant was relatively low ($k = 0.0262$ min^{-1}), which is typical of catalytic systems treating highly colored wastewater. This behavior can be mainly attributed to the strong inner filter effect (IFE), a phenomenon of light attenuation caused by competitive absorption of UV photons by MO molecules in solution [37,38]. Because MO strongly absorbs UV light, a substantial portion of the incident photons is consumed by the pollutant itself, thereby reducing the effective light flux reaching the catalyst surface and limiting the generation of reactive species. As the reaction proceeded, the concentration of MO gradually decreased, the solution color faded (Fig. 3e), and the IFE was correspondingly weakened. As a result, the effective penetration depth of UV light increased, the light-driven activation process became more efficient, and the reaction rate increased markedly in the later stage, ultimately leading to near-complete degradation.

In addition to rapid decolorization, the capability of the Fe-AR/UV/PI synergistic system for partial mineralization was evaluated by TOC analysis. While decolorization primarily reflects the destruction of chromophoric groups, TOC removal indicates the cleavage of the organic backbone and its eventual mineralization [39]. As shown in Fig. 3f, the TOC content gradually decreased during MO degradation, and a mineralization efficiency of 42.91% was achieved after 12 h of reaction. This result indicated that the synergistic system was able not only to rapidly eliminate the chromophoric structure of MO, but also to decompose its organic carbon skeleton. The TOC removal rate demonstrated the considerable potential of this system for pollutant detoxification, further confirming the partial mineralization of Fe-AR in PI (UV) activation.

The rate constant comparison shown in Fig. 4d further highlighted the remarkable advantage of the ternary synergistic system by different degradation systems towards MO degradation. The observed degradation rate constant for MO ($k = 0.1378$ min^{-1}) by Fe-AR/UV/PI reflected good catalytic activity and was higher than those reported for many recently developed heterogeneous catalytic systems, including plasmonic Au/TiO_2 under visible light ($k \approx 0.0385$ min^{-1}) [40], Z-scheme heterojunction $Zn_3In_2S_6$/FCN ($k \approx 0.0345$ min^{-1}) [41], carbon dot-modified TiO_2 composites ($k \approx 0.022$ min^{-1}) [42], microwave-assisted nZVI@N-rGOA system ($k \approx 0.0163$ min^{-1}) [43], S-scheme g-C_3N_4/ZnO/CNT nanocomposites ($k \approx 0.0088$ min^{-1}) [44], and Tm^{3+}-doped TiO_2 coatings ($k \approx 0.0028$ min^{-1}) [45]. These comparisons clearly demonstrated the superior catalytic efficiency of the established *in situ* self-activated Fe-AR/UV/PI system.

3.3. Influencing factors of the Fe-AR/UV/PI synergistic system

3.3.1. Effect of UV light intensity

As a key parameter in photo-assisted advanced oxidation processes (photo-assisted AOPs), light intensity serves as the direct driving force for the generation of reactive species [46]. In the Fe-AR/UV/PI synergistic system, increasing the UV light intensity markedly enhanced the degradation efficiency of pollutants. As shown in Fig. 4a and b, when the light intensity was increased from 30 to 60 and 90 mW cm^{-2}, the pseudo-first-order rate constant in the later stage of MO degradation (k_2) correspondingly increased from 0.1378 to 0.1680 and 0.2384 min^{-1}, respectively. This positive correlation indicated that photon flux is one of the key factors governing the catalytic reaction rate. The enhancement can be attributed to two main aspects. UV irradiation can accelerate the photoreduction of Fe(III) to Fe(II) during the catalytic reaction, thereby continuously regenerating active Fe(II) species for PI activation [47,48]. Furthermore, UV photons can excite the semiconducting iron oxyhydroxide layer formed in situ. Combined with the metastable electronic structure of amorphous alloy, the interfacial electron excitation and transfer are further accelerated [21,22].

3.3.2. Effect of PI concentration

As the precursor of reactive species, the initial concentration of PI is another key factor affecting the degradation performance of the system. As shown in Fig. 4c and d, increasing the PI concentration markedly accelerated the degradation of MO. At a concentration of 1 mmol L^{-1}, more than 98% of MO was degraded within 50 min. When the PI concentration was increased to 2 mmol L^{-1}, the required reaction time was shortened to 40 min, and further increasing the concentration to 5 mmol L^{-1} reduced the degradation time to within 30 min. Correspondingly, the pseudo-first-order rate constant in the later stage of the reaction increased substantially from 0.1106 min^{-1} at 1 mmol L^{-1} to 0.3190 min^{-1} at 5 mmol L^{-1}. These results clearly demonstrated that the PI concentration played a decisive role in controlling the generation rate

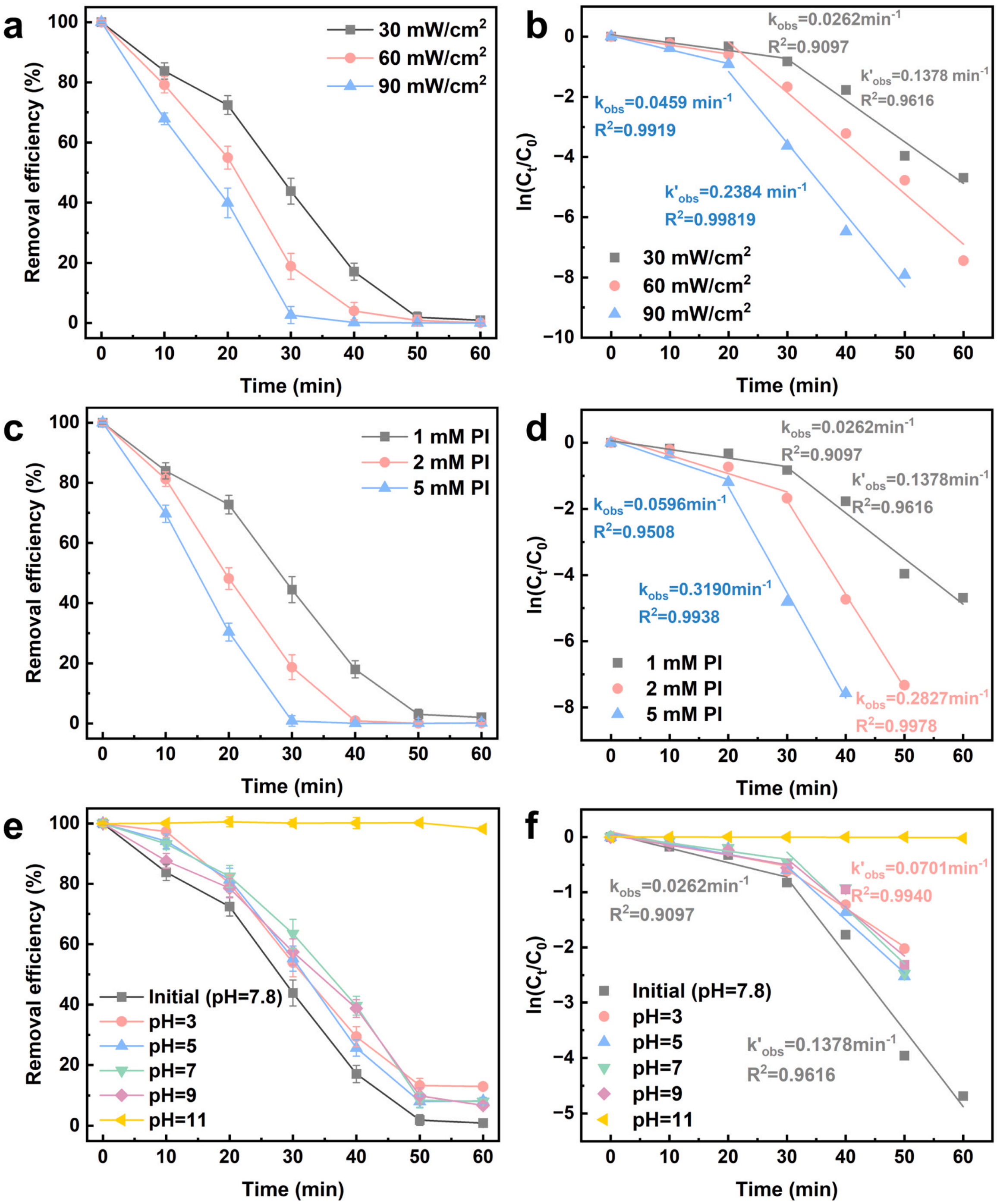

Fig. 4. (a, b) Effect of UV light intensity on degradation of MO by Fe-AR/UV/PI synergistic system and corresponding kinetic fits. (c, d) Effect of initial PI concentration on degradation of MO by Fe-AR/UV/PI synergistic system and corresponding kinetic fits. (e, f) Effect of initial pH on degradation of MO by Fe-AR/UV/PI synergistic system and corresponding kinetic fits. Experimental conditions: $[MO]_0 = 20$ mg L^{-1}. [Fe-AR] $= 1.0$ g L^{-1}.

of reactive species. It should be noted that although a positive effect of increasing PI concentration was observed within the investigated range, excessively high oxidant dosages in other AOP systems may induce self-quenching of reactive radicals, thereby inhibiting the overall reaction rate [10].

3.3.3. Effect of pH

To evaluate the practical applicability of the Fe-AR/UV/PI synergistic system in water treatment in terms of pH value, the effect of the different pH on MO degradation was systematically investigated. As shown in Fig. 4e and f, the system exhibited excellent pH tolerance over a wide range. At initial pH values of 3, 5, 7, and 9, the removal efficiency of MO remained above 87% after 60 min, while the corresponding later-stage pseudo-first-order rate constants (k_2) were all maintained at relatively high levels of 0.07–0.1 min^{-1}. This behavior overcame the limitation of conventional Fenton reactions, which are typically effective only under strongly acidic conditions.

However, when the initial pH was increased to 11, the reaction was almost completely suppressed. This inhibition can be attributed to two main factors. First, under strongly alkaline conditions, PI tended to convert into dimeric species such as $H_6IO_6^{2-}$, which exhibited lower oxidation potential and reduced reactivity [10]. Second, elevated pH promoted the rapid precipitation of iron ions as hydroxides, which can accumulate on the catalyst surface, block active sites, and hinder interfacial electron transfer, ultimately leading to catalyst deactivation [49]. Overall, the Fe-AR/UV/PI system does not require strict pH adjustment and can maintain efficient performance over a broad pH range from acidic to weakly alkaline conditions (pH 3–9), which greatly enhanced its potential for practical application in water treatment.

3.4. Characterization of surface structure and chemical state

3.4.1. EDS analysis

To elucidate the compositional changes associated with the morphological evolution during the *in situ* activation process, detailed SEM-energy dispersive spectrometry (EDS) analysis was performed on the catalyst surface. According to the quantitative EDS results, the surface of pristine Fe-AR (Fig. 5a) was relatively clean and exhibited little oxidation, consisting mainly of Fe (89.14 at%) and Si (9.66 at%). with only 1.20 at% oxygen. At this stage, the Fe:Si atomic ratio is approximately 9.2:1, which is consistent with the designed composition of the alloy ($Fe_{78}Si_9B_{13}$). However, after reaction in the Fe-AR/UV/PI system, the surface composition of the catalyst surface underwent a clear and systematic evolution. After exposure to 1 mmol L^{-1} PI, the surface became heavily oxidized, with the oxygen content increasing sharply from 1.20 to 53.55 at%, while the Fe and Si contents decreased to 42.45 and 4.00 at%, respectively. As the PI concentration was further increased to 2 and 5 mmol L^{-1}, this trend became even more pronounced, with the oxygen content reaching 58.03 at% and the Fe content correspondingly decreasing to 37.18 at%.

Combined with the corrosion pits observed in Fig. 5, these results suggested a complex surface reconstruction process. At the initial stage of the reaction, Si may underwent preferential and rapid dissolution, in a manner analogous to dealloying, which has been demonstrated to be an effective strategy for generating porous surfaces on amorphous catalysts [50]. Subsequently, iron oxides/oxyhydroxides, such as FeOOH, are gradually formed and deposited on the surface, eventually giving rise to the active surface layer and further lowering the relative proportion of Fe detected by EDS.

Overall, the progressive evolution revealed by the EDS data confirmed that the three-dimensional nanoflower-like structures observed in Fig. 5b-d are not merely the result of physical surface roughening, but instead represent a newly formed chemically active interface enriched in oxygen and iron, generated through preferential oxidation of iron and selective migration or dissolution of silicon. These results provided strong evidence for the *in situ* self-activation behavior of the catalyst, indicating that a truly active surface layer is spontaneously constructed under reaction conditions.

3.4.2. XPS analysis

To clarify the chemical basis of the catalyst's *in situ* self-activation at the atomic and electronic levels, the evolution of the surface chemical states of Fe-AR before and after reaction was systematically investigated by XPS (Fig. 6). The Fe 2p spectra reveal the valence-state evolution of the catalytically active Fe sites. As shown in Fig. 5a, the pristine Fe-AR surface contained three Fe species: metallic Fe^0 (706.78 eV, 14.54%), Fe^{2+} (710.88 eV, 56.68%), and Fe^{3+} (712.88 eV, 28.78%). This result indicated that the metallic matrix is initially covered by a native oxide/passivation layer, which is commonly observed for Fe-based alloys exposed to air. After exposure to PI under UV irridiation, the

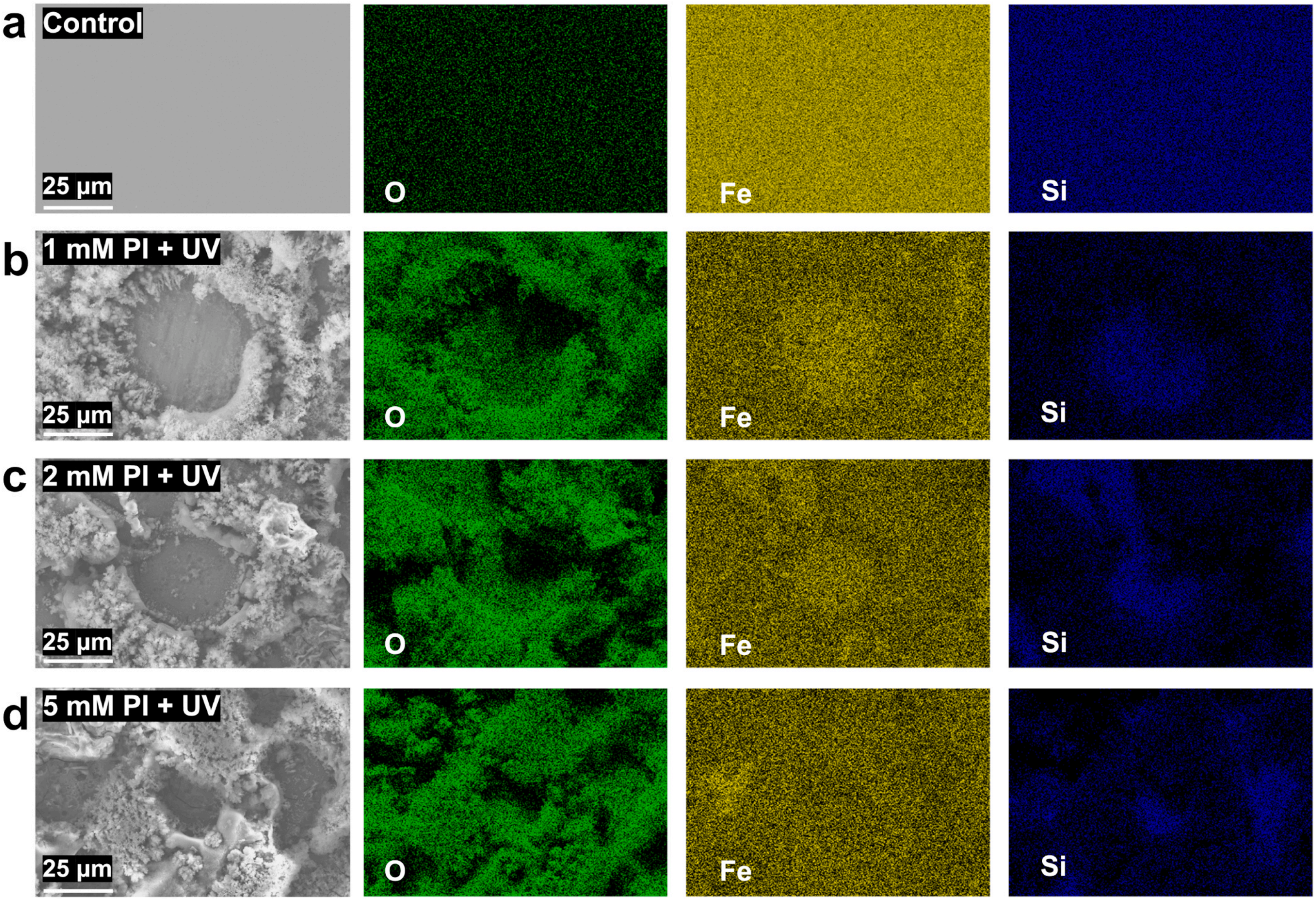

Fig. 5. (a) The SEM and EDS spectra of pristine Fe-AR with elemental distribution of O, Fe, and Si. (b-d) The SEM and EDS spectra of Fe-AR by exposure to 1, 2, and 5 mmol L^{-1} PI under UV irradiation (30 mW cm^{-2}).

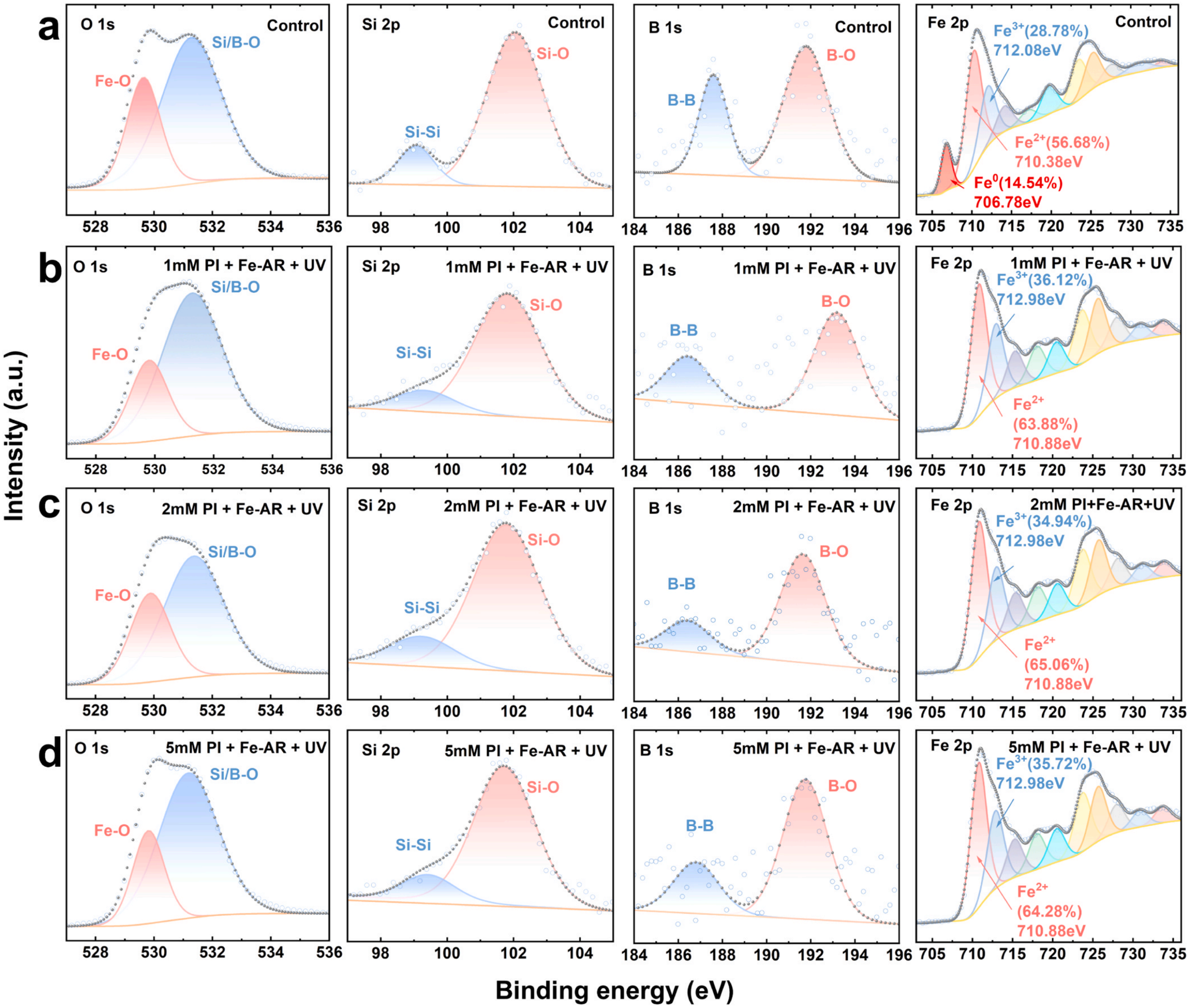

Fig. 6. The XPS spectra of (a) O 1 s, Si 2p, B 1 s and Fe 2p for the pristine Fe-AR, (b) O 1 s, Si 2p, B 1 s and Fe 2p for the Fe-AR exposure to 1 mmol L^{-1} PI under UV irradiation (30 mW cm^{-2}), (c) O 1 s, Si 2p, B 1 s and Fe 2p for the Fe-AR exposure to 2 mmol L^{-1} PI under UV irradiation (30 mW cm^{-2}), (d) O 1 s, Si 2p, B 1 s and Fe 2p for the Fe-AR exposure to 5 mmol L^{-1} PI under UV irradiation (30 mW cm^{-2}).

characteristic Fe^{0} peak was no longer detectable in samples treated under the combined action of UV and PI (Fig. 6b-d). This provided direct evidence that the surface metallic Fe fully participated in the oxidative surface reconstruction process [51]. More importantly, the reconstructed surface layer stabilized the Fe species in a dynamic equilibrium enriched in Fe^{2+}, with its relative content remaining at a high level of 63–65% under different PI concentrations. The sustained presence of abundant Fe^{2+} is essential for the efficient and continuous activation of PI. In addition, the appearance of a distinct satellite peak at approximately 719 eV in the reacted samples was characteristic of iron oxyhydroxides, confirming FeOOH as one of the major components of the newly formed active layer.

The O 1 s spectra provided further insight into the composition and evolution of the reconstructed surface layer. In the pristine sample, the O 1 s signal can be deconvoluted into two components assigned to Fe-O (31.46%) and Si/B-O (68.54%). After treatment with 1 mmol L^{-1} PI under UV irradiation, the relative proportion of the Fe-O component decreases by 15.97%, suggesting the active involvement of iron oxide species in the initial oxidation process. As the PI concentration increased further, the Fe-O proportion remained relatively stable, indicating that a stable surface layer was gradually established and that the catalyst maintained good structural stability during reaction.

The Si 2p and B 1 s spectra further revealed the evolution of metalloid species on the catalyst surface. The Si 2p results showed that the total surface Si content remained nearly unchanged after reaction. When considered together with the overall decrease in Si content detected by EDS, this observation suggested a dissolution-reprecipitation process of Si-containing species at the surface. Because XPS is highly surface-sensitive, probing only the top 2–5 nm, whereas EDS reflected the average composition over a much larger sampling depth on the micrometer scale, thereby capturing both bulk Si depletion and surface redeposition. Importantly, this selective Si leaching acted as an *in situ* dealloying process, creating the initial nanoporosity that served as a crucial spatial template for the subsequent growth of Fe-oxyhydroxide nanoflowers. Meanwhile, the B 1 s spectra showed that the proportion of metallic B-B bonds decreased from 32.85% to 28.74%, while that of oxidized B-O bonds increased from 67.01% to 71.26%, indicating further oxidation of boron during the reaction. Boron is believed to play an important role in suppressing the formation of a dense passivation layer and serving as an electron donor to facilitate the Fe(III)/Fe(II) redox cycle [33].

Overall, the XPS results clearly elucidated the chemical nature of the *in situ* self-activation process. During catalysis reaction, the catalyst surface was transformed into a functional interface dominated by iron oxyhydroxides such as FeOOH, which stabilized the surface Fe species in a Fe^{2+}-rich state favorable for PI activation. This active Fe-based layer was likely covered by an ultrathin, hydrophilic outer shell enriched in Si/B oxides or hydroxides formed through a dissolution-reprecipitation process. The resulting chemically integrated and functionally synergistic interface constituted the key structural basis for the highly efficient operation of the catalytic system.

3.4.3. XAFS analysis

To further elucidate the *in situ* self-activation mechanism at the atomic scale, Fe K-edge XAFS measurements were performed on the Fe-AR before and after reaction. The X-ray absorption near-edge structure (XANES) spectra (Fig. 7a) showed that the absorption edge positions of the reacted and pristine Fe-AR samples largely overlap and remain close to that of standard Fe foil, suggesting that the bulk phase of the catalyst retains its predominantly metallic character (Fe^0) before and after catalysis reaction. A closer examination showed that the reacted Fe-AR exhibited a slight positive shift in the near-edge absorption energy, accompanied by an increase in white-line intensity. This change indicated an increase in the unoccupied states of Fe 3*d* orbitals and partial outward electron transfer from local Fe centers during reaction, resulting in a slight increase in the average valence state of Fe in the material. This observation is consistent with the XPS results, which indicate attenuation of the outermost Fe^0 signal together with enrichment of oxidized Fe species at the surface [52].

The Fourier-transformed R-space spectra (Fig. 7b) provided further insight into the coordination reconstruction induced by reaction. The pristine Fe-AR exhibited coordination peaks at approximately 1.4 and 2.2 Å, which can be assigned to Fe-B and Fe-Fe/Fe-Si interactions, respectively, reflecting the composite coordination network characteristic of its metastable amorphous structure. After catalysis reaction, the Fe-AR not only retained the metallic-bond-related feature at 2.2 Å, but also showed an increased intensity around 1.4 Å together with the emergence of a shoulder peak near 1.8 Å. The enhancement at 1.4 Å can be attributed to the overlap between newly formed surface Fe-O bonds and the intrinsic Fe-B coordination shell, while the shoulder peak at 1.8 Å was likely associated with Fe-O/OH coordination in the reconstructed iron oxyhydroxide layer, such as FeOOH. The coexistence of a preserved metallic bulk network and newly generated surface Fe-O coordination suggested the formation of a heterogeneous interface consisting of a zero-valent metallic core and an active oxidized surface layer. Such an interfacial configuration is expected to facilitate directional electron transfer and thereby support efficient catalytic cycling.

3.5. Catalytic advantages of the amorphous structure

3.5.1. Comparison of amorphous, crystalline, and powdered Fe-based materials

To clarify the critical role of the amorphous structure in achieving high catalytic activity, the structural characteristics and surface evolution of Fe-AR, its crystallized counterpart (Fe-CR), and commercial Fe powder (Fe-P) were systematically compared before and after reaction (Fig. S2). This comparison was intended to reveal the intrinsic structural advantages of the amorphous state.

The three Fe-based materials exhibited distinctly different initial states. As shown in the XRD patterns in Fig. S2g, Fe-AR displayed a typical broad diffuse peak centered at approximately 45°, indicative of its long-range disordered atomic structure. In contrast, both the crystalline ribbon and Fe powder exhibited sharp diffraction peaks corresponding to α-Fe crystal planes, confirming their well-ordered crystalline structures. These intrinsic structural differences were also reflected in their initial surface morphologies. The Fe-AR surface (Fig. S2a) was smooth and homogeneous, whereas the crystalline ribbon (Fig. S2c) exhibited clear grain-boundary features, and the Fe powder (Fig. S2e) consisted of irregular polyhedral particles.

After exposure to identical UV/PI reaction conditions, the three materials showed markedly different surface evolution behaviors, directly highlighting the uniqueness of the amorphous structure. As described above, Fe-AR underwent the most pronounced surface reconstruction (Fig. S2b), with its initially smooth surface being transformed into a complex three-dimensional active layer composed of nanoflower-like structures, corrosion pits, and microcracks. In contrast, the crystalline ribbon (Fig. S2d) and Fe-P (Fig. S2f) exhibited only limited corrosion or slight surface deposition after reaction, while their overall morphology and structural features remained largely unchanged. This striking difference in reactivity originated from the fundamental distinctions between amorphous and crystalline materials. From a thermodynamic perspective, amorphous alloys are metastable materials produced by rapid quenching and possessed higher free energy than their crystalline counterparts [26,27]. This metastability provided a stronger thermodynamic driving force for surface activation and made them more susceptible to oxidative etching under strongly oxidizing conditions. In addition, in terms of structural and compositional uniformity, amorphous materials lacked the grain boundaries, dislocations, and other long-range defects commonly present in crystalline solids [31]. In crystalline materials, such defects often serve as preferential

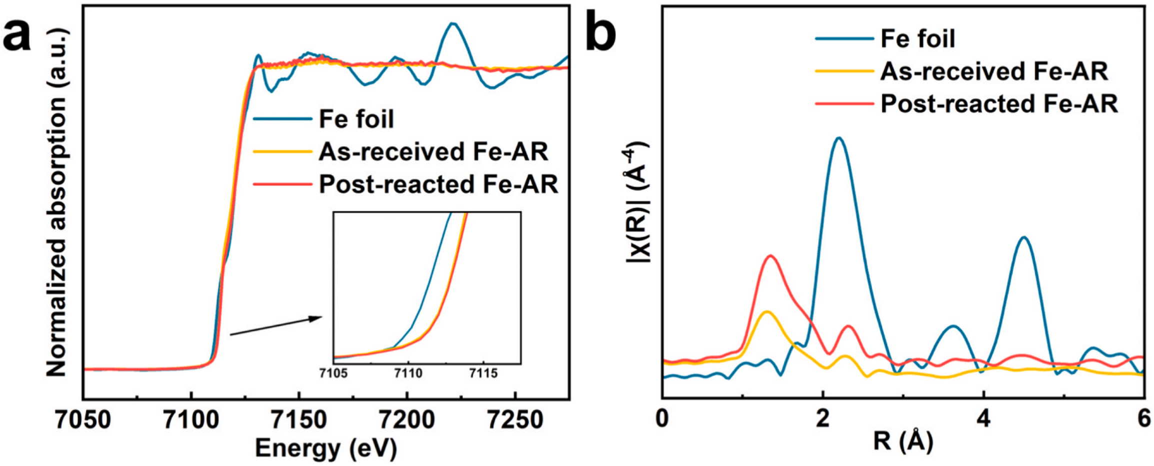

Fig. 7. (a) Normalized Fe K-edge XANES spectra and (b) Fourier-transformed EXAFS spectra in R-space of the standard Fe foil, as-received Fe-AR, and post-reacted Fe-AR ([PI] = 1 mmol L^{-1}. UV intensity = 30 mW cm^{-2}).

corrosion sites, but they can also be rapidly blocked by corrosion products, leading to local passivation and suppression of further reaction. By contrast, the uniform surface and random atomic distribution of Fe and Si in Fe-AR allowed the initial oxidative attack to occur more homogeneously across the entire surface. This uniformity was likely a prerequisite for the subsequent spontaneous and organized formation of nanoflower-like structures, rather than the irregular localized pitting typically observed in crystalline materials.

Importantly, the XRD pattern in Fig. S2h indicated that although the surface of Fe-AR underwent pronounced reconstruction, the bulk material still retained the broad diffuse peak characteristic of the amorphous state. This result suggested that the *in situ* self-activation process is mainly confined to the surface region of the catalyst, while the amorphous matrix remained intact as a stable structural support and a continuous source of active Fe species. This behavior was in sharp contrast to the relative surface inertness of the crystalline materials.

Overall, this comparative study established a clear link between the amorphous structure and the unique self-activation capability of Fe-AR.

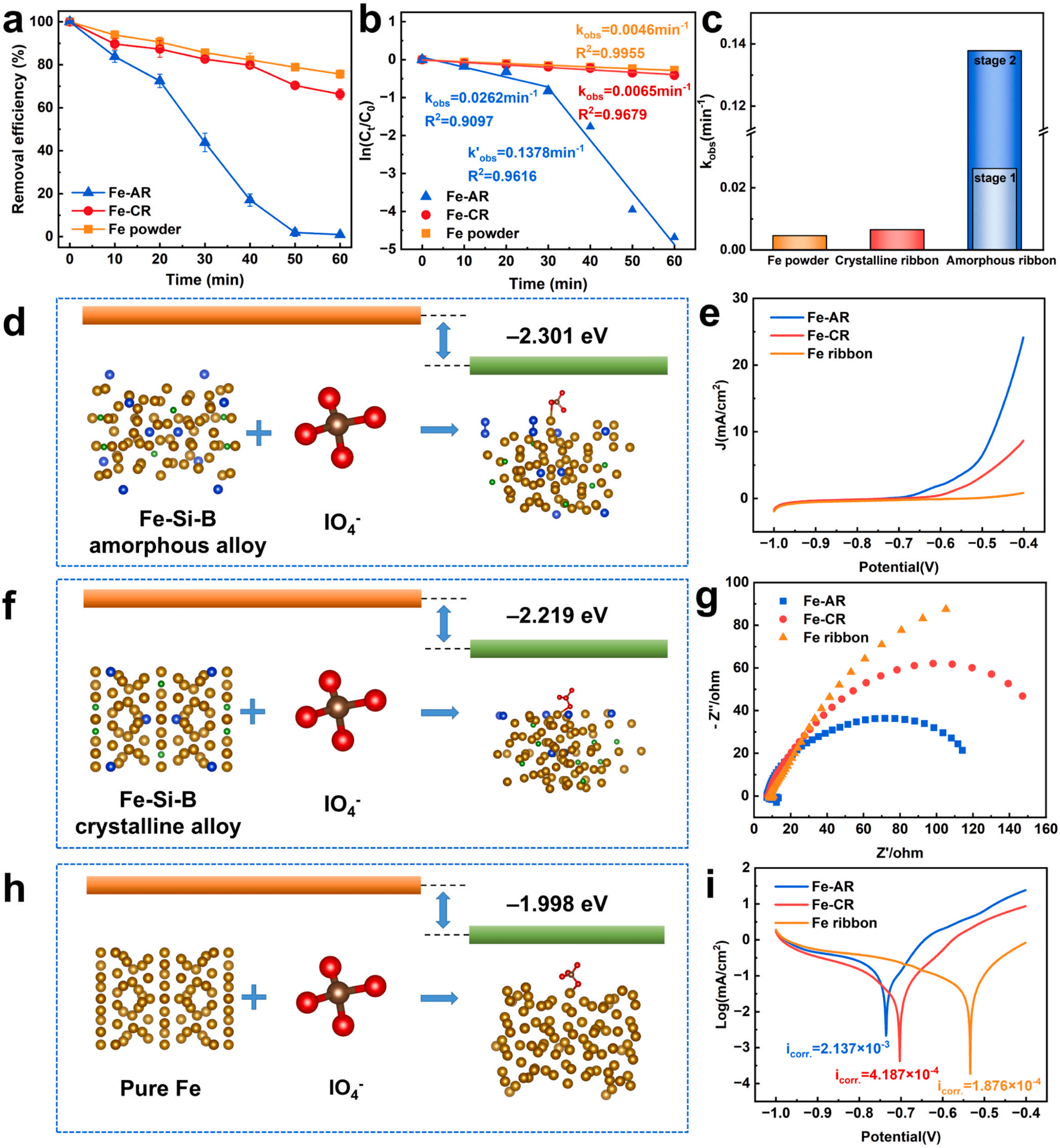

Fig. 8. (a-c) MO degradation performance and kinetics comparison for Fe-AR, Fe-CR, Fe powder (material dosage = 1 g/L, [PI] = 1 mmol L^{-1}. UV intensity = 30 mW cm^{-2}). (d, f, h) DFT calculation results of adsorption energy of Fe-Si-B amorphous alloy, Fe-Si-B crystalline alloy, and pure Fe over PI. (e, g, i) Electrochemical analysis (CV curves, Nyquist plots and Tafel curves) of Fe-AR, Fe-CR, Fe ribbon, ($[Na_2SO_4 \text{ electrolyte}]_0$ = 0.05 mol L^{-1}).

The long-range disordered structure and high-free-energy state of the amorphous alloy appeared to be the fundamental prerequisites for reaction-driven surface nanoengineering and the resulting enhancement in catalytic performance.

3.5.2. *Catalytic performance, theoretical calculations, and electrochemical analysis*

To correlate the structural and morphological differences discussed above with the pronounced disparity in catalytic performance, the three Fe-based materials were further systematically compared from three aspects: degradation efficiency, theoretical adsorption energy, and electrochemical behavior (Fig. 8).

First, the catalytic degradation results (Fig. 8a) clearly quantify the differences in performance among the three Fe-based materials. Fe-AR exhibited far superior degradation performance toward MO compared with its crystallized counterpart and commercial Fe powder. According to the pseudo-first-order kinetics fitting (Fig. 8b), the reaction rate constant (k) of Fe-AR reached 0.1378 min^{-1}, which was 21.2 and 30.0 times higher than those of the crystalline ribbon (0.0065 min^{-1}) and Fe powder (0.0046 min^{-1}), respectively (Fig. 8c), demonstrating its pronounced catalytic advantage. This large performance difference can first be attributed to the different interaction strengths between the catalyst surface and reactant molecules. To clarify this, density functional theory (DFT) calculations were performed to determine the adsorption energies of IO_4^- on the surfaces of the three materials. DFT is a powerful tool for elucidating the interactions between the unique electronic structure of materials and reactants [25]. The calculated adsorption energy (E_{ads}) of IO_4^- on the amorphous alloy surface was −2.301 eV (Fig. 8d), which is more negative than that on the crystalline alloy surface (−2.219 eV, Fig. 8 f) and pure Fe (−1.998 eV, Fig. 8 h). A more negative adsorption energy indicated stronger chemical adsorption, which not only promoted the enrichment of IO_4^- on the catalyst surface but may also facilitated its activation through stronger interfacial electronic interaction, thereby lowering the energy barrier for subsequent reaction steps. These results suggested that the unique disordered atomic arrangement and high-energy active sites of the amorphous structure were more favorable for capturing and activating PI species.

In addition to its theoretical adsorption advantage, the superior electron-transfer capability of Fe-AR was another key factor underlying its high catalytic activity, as confirmed by a series of electrochemical measurements. The Nyquist plots obtained from electrochemical impedance spectroscopy (EIS) (Fig. 8 g) show that Fe-AR exhibits the smallest semicircle diameter among the three Fe-based materials, indicating the lowest charge-transfer resistance (R_{ct}). This result suggested that electron transfer at the catalyst-solution interface is more efficient, thereby providing a more favorable pathway for catalytic cycling. The Tafel polarization curves (Fig. 8i) further quantified the electrochemical activity of the three Fe-based materials. Fe-AR exhibited the highest corrosion current density ($i_{\text{corr}} = 2.137 \times 10^{-3}$ mA cm^{-2}), far exceeding that of the crystalline ribbon ($i_{\text{corr}} = 4.187 \times 10^{-4}$ mA cm^{-2}) and Fe ribbon ($i_{\text{corr}} = 1.876 \times 10^{-4}$ mA cm^{-2}). In the specific context of advanced oxidation catalysis, the notably higher i_{corr} of the amorphous alloy fundamentally reflects its superior intrinsic surface electroactivity and highly accelerated interfacial charge transfer kinetics. This robust electrochemical property signifies that the catalyst can more efficiently facilitate continuous electron exchange with PI molecules, significantly boosting the regeneration of active surface sites and accelerating the overall catalytic redox cycle [53]. This interpretation was also consistent with the polarization behavior shown in Fig. 8e, where Fe-AR exhibited the highest current response.

Overall, the superior catalytic performance of Fe-AR can be regarded as a macroscopic manifestation of its intrinsic structural advantages. Its outstanding activity arose from the synergistic combination of stronger reactant adsorption, as supported by DFT calculations, and faster interfacial electron transfer, as confirmed by electrochemical analysis. Together, these features account for why the catalytic activity of Fe-AR far exceeded that of the crystalline ribbon and Fe powder, further highlighting the great potential of amorphous alloys as high-performance heterogeneous catalysts.

3.6. *EPR and synergistic catalytic mechanism*

To elucidate the underlying mechanism of pollutant degradation in the Fe-AR/UV/PI system, electron paramagnetic resonance (EPR) spectroscopy and reactive-species quenching experiments were systematically performed and comprehensively analyzed.

In the EPR measurements using DMPO as the spin-trapping agent, multiple radical signals were detected, featuring the typical DMPO-·OH characteristic peaks with an intensity ratio of 1:2:2:1 (Fig. 9a) [54]. As a control, the pure DMPO solution and the system with only Fe-AR showed negligible radical signals. When PI was introduced alone, typical DMPO-·OH characteristic peaks appeared, indicating the generation of a certain amount of ·OH by PI. The addition of Fe-AR to the PI system further increased the signal intensity. Ultimately, the ternary Fe-AR/UV/PI system exhibited the highest multiplet radical signals, demonstrating a synergistic enhancement in radical generation. Reactive iodine radicals such as $IO_4\cdot$ and $IO_3\cdot$ generated during PI activation are known to be unstable in aqueous solutions [55,56]. These species can rapidly undergo hydrolysis and spontaneous transformation, yielding secondary reactive oxygen species such as ·OH together with more stable iodate species [7]. In addition, the DMPO adducts of iodine-centered radicals may exhibit spectral features similar to those of DMPO-·OH, making signal overlap likely [57]. Such species transformation and spectral superposition may account for the complex multiplet signals observed in Fig. 9a. Consistently, the addition of isopropanol (IPA), a scavenger for ·OH, only partially suppressed pollutant degradation (Fig. 9c), suggesting that ·OH participated in the reaction but was not the dominant oxidizing species.

The absence of a clear EPR signal for $O_2\cdot^-$ may be attributed to the short lifetime of the DMPO-OOH adduct in aqueous solution, which can rapidly decompose or convert into the DMPO-OH adduct (Fig. S3) [57]. Nevertheless, *p*-benzoquinone (*p*-BQ) used as a scavenger for $O_2\cdot^-$, partially inhibited MO degradation (Fig. 9c), indicating that superoxide radicals were also involved in the reaction process. In the present system, $O_2\cdot^-$ may not only act as an auxiliary reactive species, but also serve as a potential intermediate that can further transform into singlet oxygen ($^1O_2$) through subsequent oxidation pathways.

When TEMP was used as the spin-trapping agent, a characteristic 1:1:1 triplet signal was observed, confirming the generation of singlet oxygen $^1O_2$ (Fig. 9b) [58]. This result is in good agreement with the quenching experiments. The addition of L-histidine (L-His), a selective scavenger for $^1O_2$, or phenol, a broad-spectrum quencher for reactive oxidizing species, inhibited the degradation reaction, with only 1.65% and 0.21% of MO removed after 60 min, respectively. It should be noted that the EPR signal intensity mainly confirms the formation of specific ROS, but it cannot be directly correlated with their relative contribution to MO degradation because of the different trapping efficiencies and spin-adduct stabilities of DMPO and TEMP. Taken together, these results suggested that $^1O_2$ is the dominant reactive species responsible for pollutant degradation in the Fe-AR/UV/PI system.

Based on the identification of the reactive species and the quenching results, a synergistic catalytic mechanism involving photo-assisted and heterogeneous activation pathways is proposed (Fig. 9d). The process is initiated by the *in situ* surface nanoengineering of the Fe-AR catalyst. This dynamic reconstruction is synergistically driven by initial PI-induced corrosive etching, subsequent micro-galvanic coupling, and UV-excited photo-electrochemical effects. Consequently, the surface underwent reconstruction, releasing Fe^{2+} active sites (Eq. 1). It is important to note that while the pristine bulk Fe-Si-B amorphous ribbon is highly metallic in nature, the *in situ* generated surface passivation layer, primarily composed of iron oxyhydroxides such as FeOOH, exhibits typical semiconductor characteristics [51]. Therefore, UV

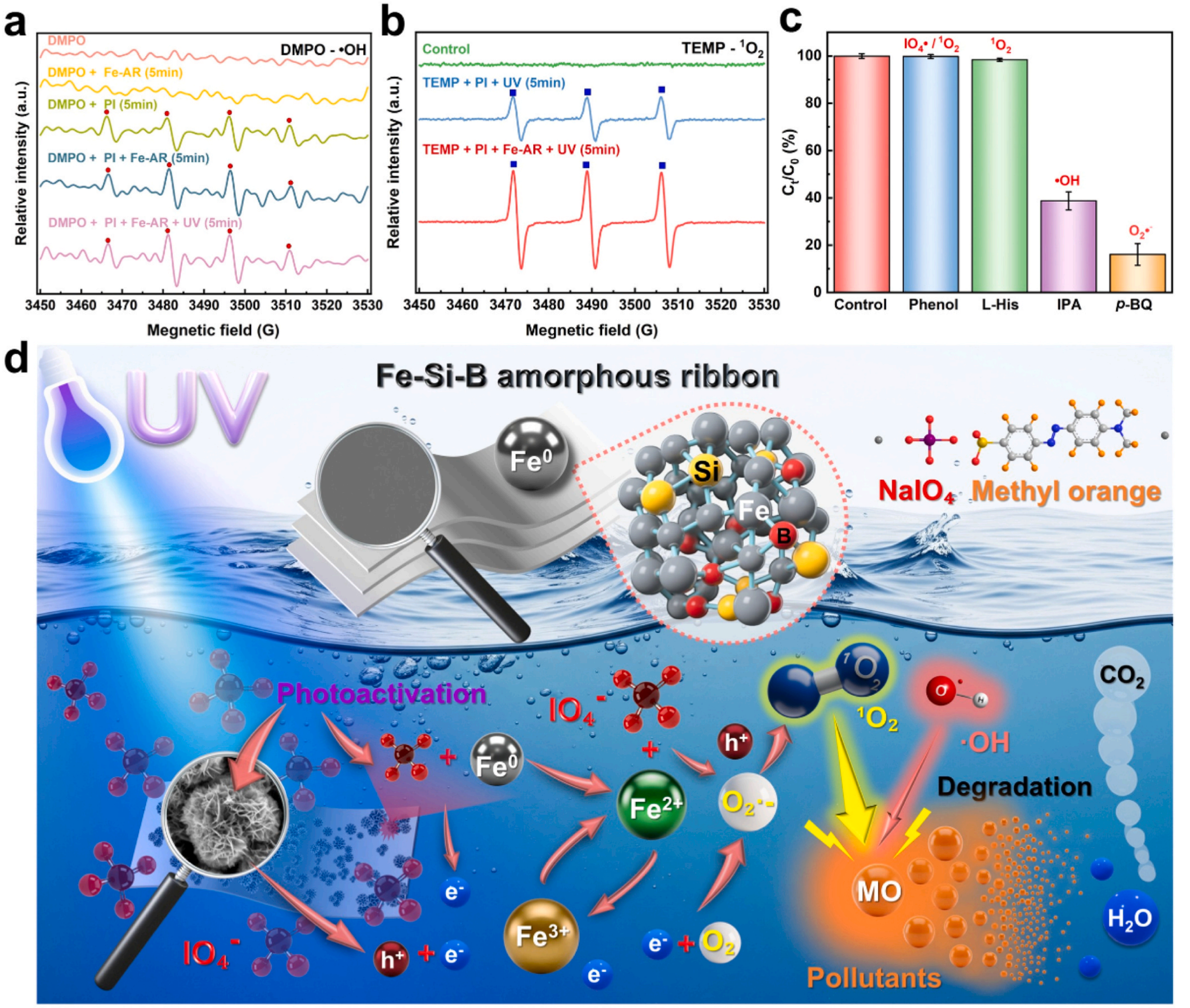

Fig. 9. (a) EPR spectra captured by DMPO in different systems ($[DMPO]_0 = 100$ mmol L^{-1}, $[PI]_0 = 1$ mmol L^{-1}, $[Fe\text{-}AR]_0 = 1$ g L^{-1}, UV intensity = 30 mW cm^{-2}). (b) EPR spectra captured by TEMP in different systems ($[TEMP]_0 = 100$ mmol L^{-1}). (c) Effects of different quenching agents on the catalysis degradation of MO by Fe-AR/UV/PI system ($[phenol]_0 = 20$ mmol L^{-1}, $[L\text{-}His]_0 = 20$ mmol L^{-1}, $[IPA]_0 = 100$ mmol L^{-1}, $[p\text{-}BQ]_0 = 100$ mmol L^{-1}). (d) The schematic diagram of the catalytic mechanism.

irradiation excited the reconstructed semiconducting Fe-AR to generate electron-hole pairs (Eq. 2). Photogenerated holes oxidized adsorbed water to produce ·OH (Eq. 3). A portion of electrons reduced dissolved oxygen to $O_2\cdot^-$ (Eq. 4). PI activation followed several pathways as direct photolysis cleaved the I-O bond to generate $IO_3\cdot$ and $O\cdot^-$ (Eq. 5) [7]. $O\cdot^-$ reacted with water to yield secondary ·OH (Eq. 6). IO_4^- reacts with ·OH or holes to form the $IO_4\cdot$ radical (Eq. 7). The reaction between released Fe^{2+} and PI generated $^1O_2$ (Eq. 8) [58]. Furthermore, guided by the dynamic metal valence transitions that critically direct reactive oxygen species evolution [59], the intermediate $O_2\cdot^-$ generated earlier undergoes rapid oxidation to continuously produce abundant $^1O_2$ (Eq. 9). This crucial transformation is synergistically driven by the oxidizing capability of photogenerated holes and the continuous iron valence redox cycle on the catalyst surface. Crucially, a dual pathway sustains the continuous Fe^{2+} regeneration. Internally, the underlying zero-valent iron acts as a sacrificial anode, undergoing continuous slow micro-galvanic corrosion to supply electrons. Concurrently on the surface, UV-excited photoelectrons directly reduce deactivated Fe^{3+} back to Fe^{2+} (Eq. 10) [60]. This dual regeneration effectively prevents catalyst passivation and sustains the iron redox cycle and $^1O_2$ generation. The generated reactive species oxidized organic pollutants (Eq. 11).

$$Fe^0 + IO_4^- + 2H^+ \rightarrow Fe^{2+} + IO_3^- + H_2O \tag{1}$$

$$Fe\text{-}AR\ (surface\ FeOOH) + h\nu \rightarrow e^- + h^+ \tag{2}$$

$$h^+ + H_2O \rightarrow \cdot OH + H^+ \tag{3}$$

$$e^- + O_2 \rightarrow O_2\cdot^- \tag{4}$$

$$IO_4^- + h\nu \rightarrow IO_3\cdot + O\cdot^- \tag{5}$$

$$O\cdot^- + H_2O \rightarrow \cdot OH + OH^- \tag{6}$$

$$IO_4^- + \cdot OH \rightarrow IO_4\cdot + OH^- \tag{7}$$

$$Fe^{2+} + IO_4^- + H_2O \rightarrow Fe^{3+} + O_2\cdot^- + IO_3^- + h^+ + e\text{-} \tag{8}$$

$$O_2\cdot^- + h^+ \rightarrow {}^1O_2 \tag{9}$$

$$Fe^{3+} + e^{-} \rightarrow Fe^{2+} \quad (10)$$

$$^{1}O_2 \,/\, \cdot OH + \text{Pollutants} \rightarrow \text{Degradation Products} \quad (11)$$

3.7. *Catalyst stability and reusability*

The long-term stability and reusability of a catalyst are critical parameters for evaluating its practical applicability [61]. As shown in Fig. 10d, Fe-AR exhibited good operational stability over eight reuse cycles of MO degradation. Notably, after eight reuse cycles, the catalyst still achieved 95.8% MO removal within 60 min, demonstrating highly stable and efficient catalytic performance.

The sustained high activity can be attributed to the formation and maintenance of a nanoengineered functional layer generated through *in situ* self-activation during reaction, as confirmed by multidimensional characterization. At the structural level, SEM images (Fig. 10a-c) clearly illustrate this evolution. The initially smooth and hydrophobic surface (Fig. 10a) was transformed after the first reaction into a rough three-dimensional nanostructure, accompanied by a marked increase in surface hydrophilicity (inset of Fig. 10b). This *in situ* formed nanoporous layer is considered essential for maintaining the long-term activity of amorphous alloys. Importantly, both the highly active nanostructure and the hydrophilic surface characteristics are largely retained even after eight reuse cycles (Fig. 10c), thereby providing a favorable interface for continuous mass transfer and catalytic reaction. Meanwhile, the XRD patterns (Fig. 10e) showed that after both the first and the eighth reuse cycles, the catalyst still retained the characteristic broad diffuse peak of the amorphous phase, indicating that the amorphous matrix remains structurally stable as the underlying support.

Cross-sectional SEM-EDS analysis (Fig. 10g-i) further revealed the dynamic nature of this stability from a depth-resolved perspective. After the first reaction (Fig. 10 h), a distinct oxygen- and iron-rich oxide layer is formed on the catalyst surface. After eight reuse cycles (Fig. 10i), this interfacial region evolved into a highly irregular and jagged morphology. Such morphological evolution suggested that the catalytic process was not limited to the outermost surface, but instead involved a dynamic inward progression of the reaction front. The jagged interfacial morphology implied that the surface active layer was gradually consumed during reaction, while the underlying amorphous matrix was continuously converted *in situ* into a newly active surface layer. In other words, the amorphous bulk can be regarded as a sacrificial atomic reservoir that continuously supplied Fe species to regenerate surface active sites, thereby sustaining the overall catalytic activity at the macroscopic level. At the chemical and elemental levels, the catalyst also exhibited good stability. The Fe 2p XPS spectrum after eight reuse cycles (Fig. 10 f) indicated that the surface still maintained a high proportion of active Fe^{2+} species (64.72%). This result suggested that the catalyst retained an efficient Fe^{2+} regeneration capability even after repeated use, thereby providing a stable chemical basis for long-term catalytic performance and sustained Fe^{2+}/Fe^{3+} redox cycling. More detailed quantitative EDS analysis further revealed the elemental evolution during long-term cycling. Compared with the pristine surface composition (Fe: 89.14 at%, Si: 9.66 at%), after eight used cycles the oxygen content increased from 1.20 to 33.20 at%, while the Si content decreased from 9.66 to 3.44 at%. As a result, the surface Fe/Si atomic ratio increases from 9.2 to 18.0. This substantial change suggested that under prolonged oxidative conditions, Si underwent sustained selective dissolution, which may facilitate the formation and renewal of the porous surface structure and thereby expose additional active sites. Such a process is consistent with a surface self-renewal mechanism that contributed to the long-term stability of the catalyst.

Overall, the good stability of this amorphous catalyst originated from a multidimensional synergistic mechanism. Structurally, it formed a highly hydrophilic nanostructured active layer that can be maintained during repeated use, while preserving a stable amorphous bulk phase as the structural backbone. Chemically, it retains a high proportion of active Fe^{2+} species that support continuous catalytic cycling. The highly stable performance observed over the eight reuse cycles highlighted its potential as a robust and durable catalytic material.

3.8. *Evaluation of broad-spectrum applicability*

The Fe-AR/UV/PI synergistic system exhibited high degradation efficiency toward MO. To further verify its broad-spectrum applicability as an advanced oxidation technology, degradation experiments were carried out using two additional representative organic pollutants with distinct structures and properties: the thiazine dye methylene blue (MB) and the antibiotic tetracycline (TC).

For MB degradation (Fig. 11a and b), a similarly strong synergistic enhancement was observed. The single PI system showed only a negligible degradation effect on MB. In the dual-component systems, PI + UV and PI + Fe-AR achieved degradation efficiencies of 91.18% and 23.06% within 60 min, respectively. The relatively high performance of the PI + UV system can be attributed to PI photolysis under UV irradiation, whereas the modest activity of the PI + Fe-AR system likely resulted from the limited activation of PI by Fe-AR. Notably, when Fe-AR, PI, and UV irradiation were combined to form the ternary synergistic system, MB degradation was further accelerated, reaching a removal efficiency of 96.45% within 60 min. The corresponding apparent rate constant (k) reached 0.0601 min^{-1} ((Fig. 11b), which was higher than those of the PI + UV system (0.0412 min^{-1}) and the PI + Fe-AR system (0.0044 min^{-1}). Because MB mainly absorbs visible rather than UV light, the inner filter effect is negligible in this system.

For TC, a typical antibiotic known to be difficult to remove effectively by conventional biological treatment processes, the Fe-AR/UV/PI system also demonstrated good degradation performance (Fig. 11c and Fig. 11d). Within 60 min, the degradation efficiencies of UV irradiation alone and PI alone were both below 10%. The dual-component PI + UV system exhibited improved activity, achieving a degradation efficiency of 54.19% with a rate constant of 0.0253 min^{-1}. However, upon introducing Fe-AR to construct a ternary synergistic system, TC was almost completely degraded within 60 min, and the apparent rate constant increased to 0.0488 min^{-1} (Fig. 11d), nearly twice that of the PI + UV system. These results indicated that even for pollutants that were already susceptible to the UV/PI process, the incorporation of the amorphous alloy can further enhance the overall degradation efficiency via its unique Fe(II)-mediated activation pathway, which operated in parallel with the photoactivation pathway.

To further evaluate practical applicability, the catalysis degradation was tested in a real water matrix containing NOM and common anions (e.g., Cl^{-}, HCO_3^{-}). The system maintained a 98.78% removal efficiency (Fig. S5), confirming its anti-interference capability.

As shown in Fig. 11e, within 60 min, the removal efficiencies for the azo dye MO, the thiazine dye MB, and the antibiotic TC reached 99.08%, 96.45%, and 94.09%, respectively. According to the pseudo-first-order degradation kinetics fitting results (Fig. 11f), the corresponding apparent degradation rate constants (k) for MO, MB, and TC were 0.1378 min^{-1}, 0.0601 min^{-1}, and 0.0488 min^{-1}, respectively. The difference in degradation rates ($k_{MO} > k_{MB} > k_{TC}$) can be mainly attributed to differences in the molecular structures of the target pollutants and their distinct reactivities toward the multiple reactive species generated in the system, such as $^{1}O_2$, and $\cdot OH$.

Overall, the results obtained for three representative organic pollutants with different chemical structures and properties led to a consistent conclusion: the degradation capability of any single-component system or dual-component combination is relatively limited, whereas the synergistic combination of Fe-AR, PI, and UV irradiation enabled rapid and efficient pollutant degradation. These findings demonstrated the broad-spectrum applicability of the Fe-AR/UV/PI system and further highlighted the potential of this ternary catalytic system for practical water treatment applications. Importantly,

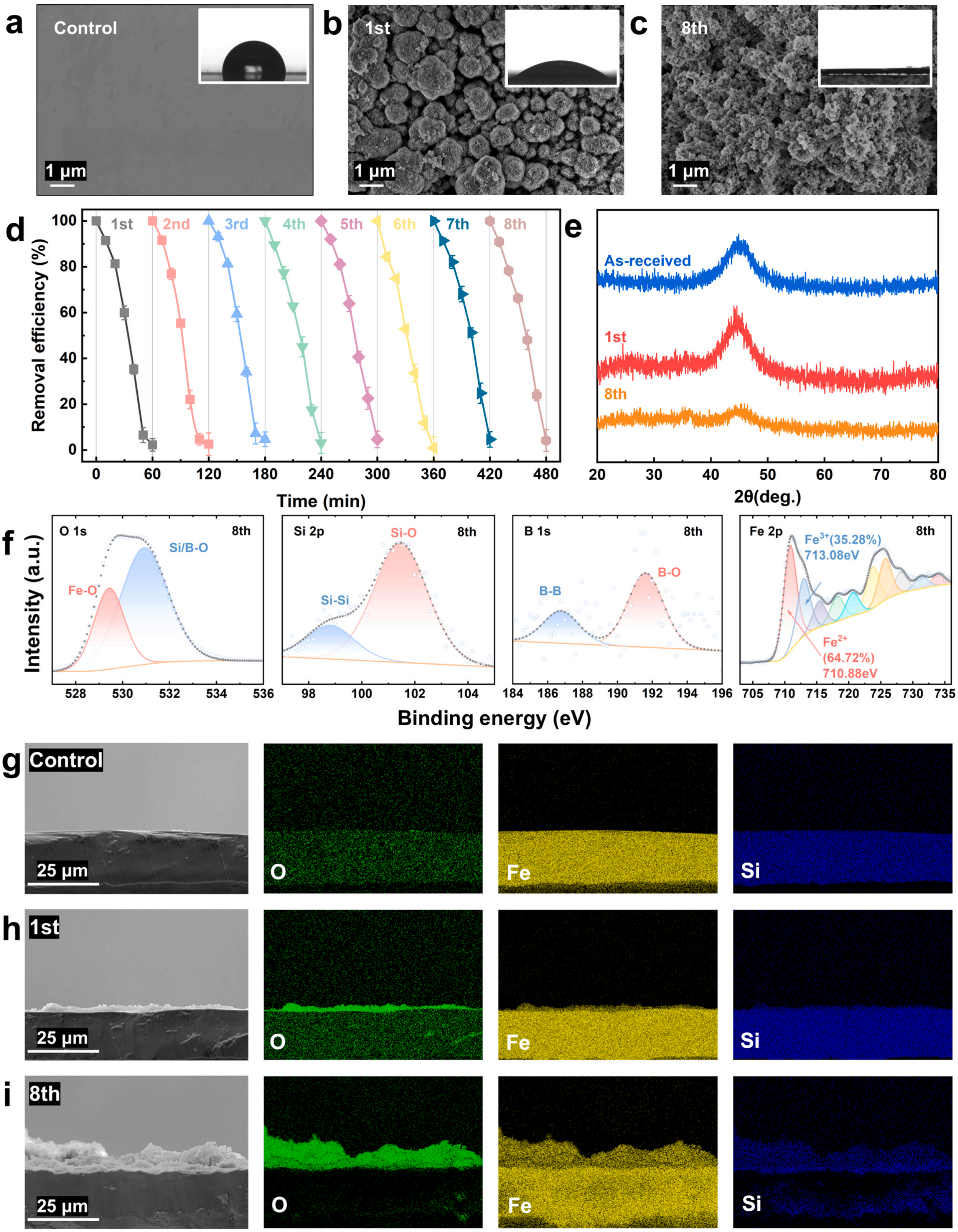

Fig. 10. (a-c) SEM spectra and water contact angles (inset graph) of as-received, once-reacted and 8th-reacted Fe-AR. (d) Reusability test for MO degradation in 8 reuse cycles. (e) XRD patterns of as-received, once-reacted and 8th-reacted Fe-AR. (f) XPS spectra of Fe-AR after 8 reuse cycles. (g-i) Cross-sectional SEM-EDS spectra of as-received, once-reacted and 8th-reacted Fe-AR. (Fe-AR dosage = 1 g/L, [PI] = 1 mmol L^{-1}. UV intensity = 30 mW cm^{-2}).

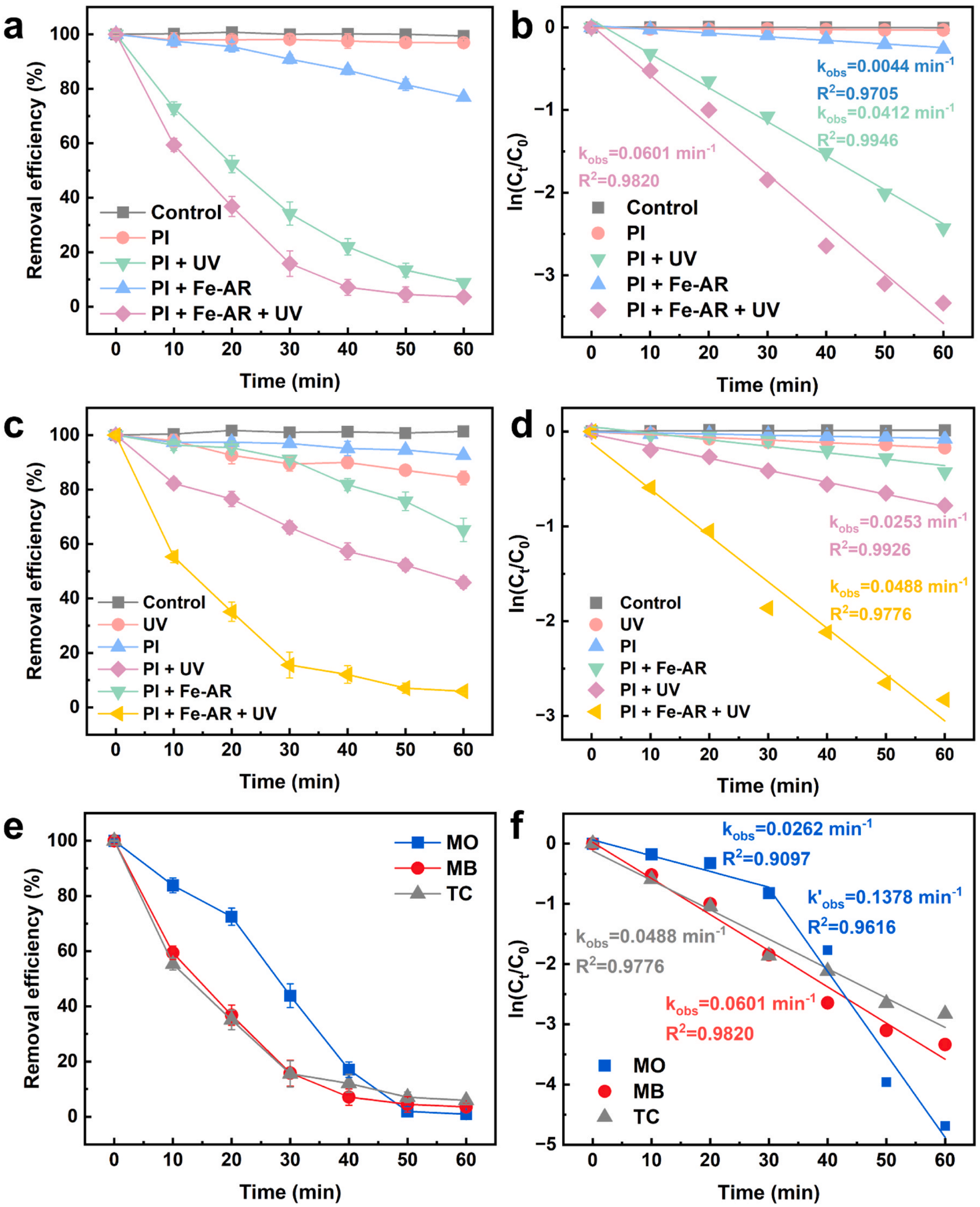

Fig. 11. (a) Degradation curves of MB in different systems. (b) Pseudo-first-order kinetic fits for MB degradation. (c) Degradation curves of TC in different systems. (d) Pseudo-first-order kinetic fits for TC degradation. (e) Degradation curves of the three pollutants (MO, MB, TC) in the Fe-AR/UV/PI synergistic system. (f) Pseudo-first-order kinetic fittings of (e), Experimental conditions: $[\text{MB}]_0 = 20\ \text{mg L}^{-1}$, $[\text{TC}]_0 = 40\ \text{mg L}^{-1}$. $[\text{Fe-AR}] = 1.0\ \text{g L}^{-1}$. $[\text{PI}] = 1\ \text{mmol L}^{-1}$. UV intensity $= 30\ \text{mW cm}^{-2}$.

the catalyst exhibited no mass loss but a slight mass increase (2.3%) after the reaction, confirming its macroscopic integrity and the *in situ* incorporation of surface oxygen. Furthermore, the low iron leaching (66.32 μg/L, well below the 0.3 mg/L WHO limit) effectively minimizes the risk of secondary metal pollution.

4. Conclusion

In summary, a highly efficient Fe-AR/UV/PI system was developed for the degradation of organic pollutants in water. Under the optimal conditions of 1 mmol L^{-1} PI and 30 mW cm^{-2} UV intensity, and an initial pH of 7.8, the system achieved 98.10% removal of MO within (20 mg L^{-1}) 50 min, with an apparent rate constant of 0.1378 min^{-1}, which was much higher than those of the crystalline ribbon and commercial Fe powder. It also showed good applicability toward MB and TC. The superior catalytic performance originated from a reaction-driven *in situ* self-activation process. During reaction, the initially smooth Fe-AR surface evolved into a nanostructured and highly hydrophilic active interface. This reconstruction was accompanied by the formation of oxygen-rich iron oxyhydroxide species, enrichment of Fe^{2+} active sites, and retention of the amorphous bulk structure. In addition, the catalyst maintained over 95.8% degradation efficiency after eight reuse cycles, confirming its excellent stability and reusability. Mechanistic studies indicated that $^1O_2$ was the dominant reactive species, while ·OH and $O_2{\cdot}^-$ served as auxiliary species. Overall, this work provides an effective strategy for PI-based advanced oxidation and offers new insight into the design of self-activating Fe-based catalytic materials for water treatment.

CRediT authorship contribution statement

Kunheng Zou: Writing – original draft, Investigation, Formal analysis. **Zhenxuan Zhang:** Writing – review & editing, Supervision, Methodology, Funding acquisition, Conceptualization. **Chaoqun Pei:** Methodology. **Xiong Liang:** Writing – review & editing, Methodology, Funding acquisition, Conceptualization. **Jiang Ma:** Writing – review & editing, Methodology, Conceptualization. **Yujian Li:** Investigation. **Yu Zhang:** Investigation. **Mengting Yang:** Conceptualization. **Jie Dong:** Funding acquisition, Conceptualization.

Declaration of Competing Interest

The authors declare that they have no known competing financial interests or personal relationships that could have appeared to influence the work reported in this paper.

Acknowledgements

The work was supported by the National Natural Science Foundation of China (Grant Nr. 52271150, 52201185, 52571190), Shenzhen Science and Technology Program (JCYJ20240813141413018), Guangdong Basic and Applied Basic Research Foundation (2026A1515011906). The authors thank the assistance on microscope observation received from the Electron Microscope Center of the Shenzhen University.

Appendix A. Supporting information

Supplementary data associated with this article can be found in the online version at doi:10.1016/j.colsurfa.2026.141158.

Data availability

Data will be made available on request.

References

[1] Y. Lu, X. Zhou, Y. Zheng, H. Yang, W. Cao, How far do we still need to go with antibiotics in aquatic environments? Antibiotic occurrence, chemical-free or chemical-limited strategies, key challenges, and future perspectives, Water Res. 275 (2025) 123179, https://doi.org/10.1016/j.watres.2025.123179.

[2] J. Lin, W. Ye, M. Xie, D.H. Seo, J. Luo, Y. Wan, B. Van der Bruggen, Environmental impacts and remediation of dye-containing wastewater, Nat. Rev. Earth Environ. 4 (2023) 785–803, https://doi.org/10.1038/s43017-023-00489-8.

[3] H. Luo, Y. Zeng, D. He, X. Pan, Application of iron-based materials in heterogeneous advanced oxidation processes for wastewater treatment: A review, Chem. Eng. J. 407 (2021) 127191, https://doi.org/10.1016/j.cej.2020.127191.

[4] Q. Feng, K. Wang, X. Li, X. Zhao, H. Sun, S. Ning, L. Wang, Catalytic degradation of methylene blue by iron-based amorphous alloys: Parameter optimization and free radical pathways, J. Alloy. Compd. 1057 (2026) 186910, https://doi.org/10.1016/j.jallcom.2026.186910.

[5] Z. Leng, L. Tang, P. Zheng, Y. Huang, X. Zhang, Y. Zheng, R. Lin, Q. Guo, W. Dai, W. Lin, Iron anode-activated peroxymonosulfate for benzohydroxamic acid degradation: Dominance of non-radical pathways and mechanistic insights, Colloids Surf. A 728 (2026) 138571, https://doi.org/10.1016/j.colsurfa.2025.138571.

[6] Z. Jia, J. Kang, W.C. Zhang, W.M. Wang, C. Yang, H. Sun, D. Habibi, L.C. Zhang, Surface aging behaviour of Fe-based amorphous alloys as catalysts during heterogeneous photo Fenton-like process for water treatment, Appl. Catal. B-Environ. 204 (2017) 537–547, https://doi.org/10.1016/j.apcatb.2016.12.001.

[7] Y. Zong, Y. Shao, Y. Zeng, B. Shao, L. Xu, Z. Zhao, W. Liu, D. Wu, Enhanced Oxidation of Organic Contaminants by Iron(II)-Activated Periodate: The Significance of High-Valent Iron-Oxo Species, Environ. Sci. Technol. 55 (2021) 7634–7642, https://doi.org/10.1021/acs.est.1c00375.

[8] S. Hu, T. Gong, Q. Xian, J. Wang, J. Ma, Z. Li, J. Yin, B. Zhang, B. Xu, Formation of iodinated trihalomethanes and haloacetic acids from aromatic iodinated disinfection byproducts during chloramination, Water Res. 147 (2018) 254–263, https://doi.org/10.1016/j.watres.2018.09.058.

[9] Y. Chen, X. Ge, J. Li, Z.B. Zhang, Z. Li, Anchored atomic Ru-O_4 architecture enables ultra-effective Fe(VI) activation via avoiding Fe(VI) self-decay for water purification, Nat. Commun. 16 (2025) 7509, https://doi.org/10.1038/s41467-025-62930-4.

[10] B. Yang, Q. Ma, J. Hao, J. Huang, Q. Wang, D. Wang, J. Zhang, Periodate-based advanced oxidation processes: A review focusing on the overlooked role of high-valent iron and manganese species, Chemosphere 337 (2023) 139442, https://doi.org/10.1016/j.chemosphere.2023.139442.

[11] J. Yue, W. Guo, S. Liang, X. Du, Z. Li, X. Wang, B. Zhang, J. Li, Comparative study on the degradation of sucralose by UV/persulfate and UV/periodate processes: Performance, dechlorination, and technical feasibility, J. Hazard. Mater. 492 (2025) 138313, https://doi.org/10.1016/j.jhazmat.2025.138313.

[12] F. Yang, D. Li, M. An, Y. Peng, Y. Ding, K. Lv, Y. Zong, D. Wu, M. Feng, S. Wang, Hydrogen-bonding with phenols mediated periodate activation under visible light: Dissolved oxygen dependent production of reactive species, Appl. Catal. B-Environ. 377 (2025) 125497, https://doi.org/10.1016/j.apcatb.2025.125497.

[13] E.-T. Yun, H.-Y. Yoo, W. Kim, H.-E. Kim, G. Kang, H. Lee, S. Lee, T. Park, C. Lee, J.-H. Kim, J. Lee, Visible-light-induced activation of periodate that mimics dye-sensitization of TiO_2: Simultaneous decolorization of dyes and production of oxidizing radicals, Appl. Catal. B-Environ. 203 (2017) 475–484, https://doi.org/10.1016/j.apcatb.2016.10.029.

[14] B. Zhang, Z. Li, F. Liu, X. Zhang, Y. Hou, M. Tong, Green and efficient disinfection of antibiotic-resistant bacteria via PI/H_2O_2 homogeneous system, Water Res. 280 (2025) 123468, https://doi.org/10.1016/j.watres.2025.123468.

[15] K. Xu, Z. Zhu, C. Hu, J. Zheng, H. Peng, B. Liu, Superior degradation of organic contaminants by the UV/$CoFe_2O_4$/PI system: Kinetics, pathways, mechanisms and DFT calculation, Sep. Purif. Technol. 336 (2024) 126197, https://doi.org/10.1016/j.seppur.2023.126197.

[16] D. Guo, Y. Yao, S. You, L. Jin, P. Lu, Y. Liu, Ultrafast degradation of micropollutants in water via electro-periodate activation catalyzed by nanoconfined Fe_2O_3, Appl. Catal. B-Environ. 309 (2022) 121289, https://doi.org/10.1016/j.jhazmat.2023.131506.

[17] Y. Wu, X. Tan, J. Zhao, J. Ma, alpha-Fe_2O_3 mediated periodate activation for selective degradation of phenolic compounds via electron transfer pathway under visible irradiation, J. Hazard. Mater. 454 (2023) 131506, https://doi.org/10.1016/j.jhazmat.2023.131506.

[18] Y. Li, J. Wang, Z. Wei, W. Li, W. Duan, X. Feng, Q. Ma, Q. Zhang, H. Chen, X. Wu, Effective periodate activation by peculiar Cu_2O nanocrystal for antibiotics degradation: The critical role of structure and underlying mechanism study, Appl. Catal. B-Environ. 341 (2024) 123351, https://doi.org/10.1016/j.apcatb.2023.123351.

[19] S. Liu, S. Liu, T. Wang, L. Yang, L. Li, X. Wu, Z. Si, R. Ran, H. Wu, Visible light assisted periodate activation with porous C_3N_5 for tetracycline degradation: Enhanced electron-hole separation and reactive oxygen species formation, Chem. Eng. J. 498 (2024) 155739, https://doi.org/10.1016/j.cej.2024.155739.

[20] Q. Tang, B. Wu, X. Huang, W. Ren, L. Liu, L. Tian, Y. Chen, L.S. Zhang, Q. Sun, Z. Kang, T. Ma, J.P. Zou, Electron transfer mediated activation of periodate by contaminants to generate $^1O_2$ by charge-confined single-atom catalyst, Nat. Commun. 15 (2024) 9549, https://doi.org/10.1038/s41467-024-53941-8.

[21] Q. Chen, H. Di, Z. Qi, Z. Wang, Z. Song, Z. Guo, X. Lu, Y. Li, L.-C. Zhang, W. Wang, Ternary metallic glass in unique atomic coordination structure and high energy state contributing to efficient photocatalytic degradation activity, J. Mater. Sci. Technol. 232 (2025) 1–13, https://doi.org/10.1016/j.jmst.2024.12.085.

[22] S.X. Liang, Z. Jia, W.C. Zhang, X.F. Li, W.M. Wang, H.C. Lin, L.C. Zhang, Ultrafast activation efficiency of three peroxides by $Fe_{78}Si_9B_{13}$ metallic glass under photo-enhanced catalytic oxidation: A comparative study, Appl. Catal. B-Environ. 221 (2018) 108–118, https://doi.org/10.1016/j.apcatb.2017.09.007.

[23] Z. Zhang, L. Qiu, Y. Li, Q. Zhu, M. Yang, A. Inoue, X. Liang, J. Ma, Metallic glass-based advanced oxidation processes in formation control of disinfection by-products in drinking water treatment, Sep. Purif. Technol. 378 (2025) 134626, https://doi.org/10.1016/j.seppur.2025.134626.

[24] Y. Li, Y. Liu, Y. Zhan, Y. Zhang, X. Zhao, M. Yang, W. Ruan, Z. Zhang, X. Liang, J. Ma, Peracetic acid-induced nanoengineering of Fe-based metallic glass ribbon in application of efficient drinking water treatment, Appl. Catal. B-Environ. 355 (2024) 124161, https://doi.org/10.1016/j.apcatb.2024.124161.

[25] Y. Liu, S. Huang, J. Lu, S. Niu, P.K. Shen, Z. Hu, P. Tsiakaras, S. Gao, $Ni_{0.25}Cu_{0.5}Sn_{0.25}$ Nanometallic Glasses As Highly Efficient Catalyst for Electrochemical Nitrate Reduction to Ammonia, Adv. Funct. Mater. 34 (2024) 2411325, https://doi.org/10.1002/adfm.202411325.

[26] Z. Jia, X. Duan, P. Qin, W. Zhang, W. Wang, C. Yang, H. Sun, S. Wang, L.C. Zhang, Disordered Atomic Packing Structure of Metallic Glass: Toward Ultrafast Hydroxyl Radicals Production Rate and Strong Electron Transfer Ability in Catalytic Performance, Adv. Funct. Mater. 27 (2017) 1702258, https://doi.org/10.1002/adfm.201702258.

[27] S. Sohrabi, J. Fu, L. Li, Y. Zhang, X. Li, F. Sun, J. Ma, W.H. Wang, Manufacturing of metallic glass components: Processes, structures and properties, Prog. Mater. Sci. 144 (2024) 101283, https://doi.org/10.1016/j.pmatsci.2024.101283.

[28] S.X. Liang, Z. Jia, Y.J. Liu, W. Zhang, W. Wang, J. Lu, L.C. Zhang, Compelling Rejuvenated Catalytic Performance in Metallic Glasses, Adv. Mater. 30 (2018) e1802764, https://doi.org/10.1002/adma.201802764.

[29] Z. Jia, Q. Wang, L. Sun, Q. Wang, L.C. Zhang, G. Wu, J.H. Luan, Z.B. Jiao, A. Wang, S.X. Liang, M. Gu, J. Lu, Attractive In Situ Self-Reconstructed Hierarchical Gradient Structure of Metallic Glass for High Efficiency and Remarkable Stability in Catalytic Performance, Adv. Funct. Mater. 29 (2019) 1807857, https://doi.org/10.1002/adfm.201807857.

[30] R. Montenegro, J.M. Luque, P. Ortega-Columbrans, B. Ferrari, A. Rodríguez, Z. González, Tailoring CNF-TiO_2-g-C_3N_4 hybrid aerogels via surface functionalization for efficient visible-light photocatalytic degradation of methyl orange, Colloids Surf. A 735 (2026) 139477, https://doi.org/10.1016/j.colsurfa.2026.139477.

[31] S. Jiang, G. Cao, Z. Jia, L. Sun, C. Wang, H. Fan, Y. Wang, W. Xu, Y. Cui, Z. Ning, J. Sun, J. Li, X. Tang, H. Liang, E. Peng, A Superb Iron-Based Glassy-Crystal Alloy Fiber as an Ultrafast and Stable Catalyst for Advanced Oxidation, Adv. Fiber Mater. 6 (2024) 1483–1494, https://doi.org/10.1007/s42765-024-00426-4.

[32] S.X. Liang, Q. Zhang, Z. Jia, W. Zhang, W. Wang, L.C. Zhang, Tailoring surface morphology of heterostructured iron-based Fenton catalyst for highly improved catalytic activity, J. Colloid Interface Sci. 581 (2021) 860–873, https://doi.org/10.1016/j, jcis.2020.07.138.

[33] Y. Liu, X. Guo, J. Fu, Z. Qian, X. Liu, W. Liang, $Fe_{78}Si_9B_{13}$ amorphous alloys enhancement thermal catalytic activation of peroxydisulfate for ciprofloxacin degradation, Sep. Purif. Technol. 383 (2026), https://doi.org/10.1016/j.seppur.2025.136208.

[34] Y. Zheng, Y. Du, J. Li, Z. Liu, Y. Wu, Z. Mayu, L. Lu, J. Hu, H. Hou, Q. Zhu, Efficient mineralization of azo dye in a Nd-doped TiO_2 photoanode-coupled microbial fuel cell: Performance, microbiology and mechanism, Sep. Purif. Technol. 388 (2026) 136745, https://doi.org/10.1016/j.seppur.2026.136745.

[35] K. Shi, G. Qian, Y. Gu, W. Yi, X. Li, M. Li, Y. Zhu, R. Ding, H. Yao, Oxygen vacancy-rich 2D/2D S-scheme photocatalyst CN/BiOBr-OV for efficient azo dye degradation, Sep. Purif. Technol. 360 (2025) 131092, https://doi.org/10.1016/j.seppur.2024.131092.

[36] J. Yin, H. Zhang, M. Luo, J. Zhao, B. Huang, P. Chen, Z. Cai, Y. Yuan, Y. Liu, C. He, B. Lai, Regulating the dominant reactive oxygen species from Fe(IV)-oxo to 1O2 by deprotonation of Fe(IV)-oxo in electro-Fe(II)/periodate system, Chem. Eng. J. 497 (2024) 154896, https://doi.org/10.1016/j.cej.2024.154896.

[37] B. Wu, R. Yin, G. Zhang, C. Yu, S. Zhang, Effects of water chemistry on decolorization in three photochemical processes: Pro and cons of the UV/AA process, Water Res. 105 (2016) 568–574, https://doi.org/10.1016/j.watres.2016.09.037.

[38] A.V. Fonin, A.I. Sulatskaya, I.M. Kuznetsova, K.K. Turoverov, Fluorescence of dyes in solutions with high absorbance. Inner filter effect correction, PLoS. One 9 (2014) e103878, https://doi.org/10.1371/journal.pone.0103878.

[39] F. Polesel, H.R. Andersen, S. Trapp, B.G. Plosz, Removal of Antibiotics in Biological Wastewater Treatment Systems-A Critical Assessment Using the Activated Sludge Modeling Framework for Xenobiotics (ASM-X), Environ. Sci. Technol. 50 (2016) 10316–10334, https://doi.org/10.1021/acs.est.6b01899.

[40] Z. Wei, L. Wu, X. Yue, H. Mu, Z. Li, Y. Chang, M. Janczarek, S. Juodkazis, E. Kowalska, Titania nanoengineering towards efficient plasmonic photocatalysis: Mono- and bi-metal-modified mesoporous microballs built of faceted anatase, Appl. Catal. B-Environ. 345 (2024) 123654, https://doi.org/10.1016/j.apcatb.2023.123654.

[41] Y. Wu, H. Wang, W. Tu, Y. Liu, S. Wu, Y.Z. Tan, J.W. Chew, Construction of hierarchical 2D-2D $Zn_3In_2S_6$/fluorinated polymeric carbon nitride nanosheets photocatalyst for boosting photocatalytic degradation and hydrogen production performance, Appl. Catal. B-Environ. 233 (2018) 58–69, https://doi.org/10.1016/j.apcatb.2018.03.105.

[42] S. Cong, J. Cai, X. Li, J. You, L. Wang, X. Wang, Direct Z-Scheme Xylan-Based Carbon Dots@TiO2-x Nanocomposites for Visible Light Driven Photocatalytic of Dye Degradation and Antibacterial, Adv. Funct. Mater. 34 (2024) 2401540, https://doi.org/10.1002/adfm.202401540.

[43] P. Zhang, X. Meng, M. Fan, S. Wu, C. Wang, X. Shang, H. Jia, H. Sun, Customized design of nZVI supported on an N-doped reduced graphene oxide aerogel for microwave-assisted superefficient degradation of imidacloprid in wastewater, Appl. Catal. B-Environ. 340 (2024) 123258, https://doi.org/10.1016/j.apcatb.2023.123258.

[44] M. Nejadramezan, A. Ajami, S. Sheibani, Role of carbon nanotubes in boosting photocatalytic hydrogen production and pollutants degradation within S-Scheme g-C_3N_4/ZnO nanocomposite, Environ. Res. 284 (2025) 122176, https://doi.org/10.1016/j.envres.2025.122176.

[45] D.A. Torres-Ceron, S. Stojadinović, N. Radić, S. Amaya-Roncancio, J.P. Velasquez-Tamayo, V. Benavides-Palacios, A. Fattah-Alhosseini, E. Restrepo-Parra, Study of Tm^{3+} incorporation in TiO_2 coatings formed by plasma electrolytic oxidation at various process durations: characterization, simulation, and photocatalytic application, Appl. Surf. Sci. 713 (2025) 164338, https://doi.org/10.1016/j.apsusc.2025.164338.

[46] T. Hao, H. Xu, S. Sun, Y. Yuan, Q. Qin, M. Li, X. Ren, G. Shao, H. Wang, H. Lu, Synergy effect of sulfite, visible light, and catalyst in highly efficient photocatalytic degradation of methyl orange with sulfite activation by $ZnxMg_3$-xAl-LDH/g-C_3N_4 composite: Performances, roles, and mechanism, Colloids Surf. A 728 (2026) 138570, https://doi.org/10.1016/j.colsurfa.2025.138570.

[47] X. Zhang, M. Kamali, T. Uleners, J. Symus, S. Zhang, Z. Liu, M.E.V. Costa, L. Appels, D. Cabooter, R. Dewil, UV/TiO_2/periodate system for the degradation of organic pollutants – Kinetics, mechanisms and toxicity study, Chem. Eng. J. 449 (2022) 137680, https://doi.org/10.1016/j.cej.2022.137680.

[48] Y. Yuan, W. Wang, M. Nie, C. Yan, P. Wang, M. Ding, Visible light-mediated activation of periodate for bisphenol A degradation in the presence of Fe^{3+} and gallic acid at neutral pH, Chem. Eng. J. 479 (2024) 147541, https://doi.org/10.1016/j.cej.2023.147541.

[49] T. Chen, Y. Sun, H. Dong, J. Chen, Y. Yu, Z. Ao, X. Guan, Understanding the Importance of Periodate Species in the pH-Dependent Degradation of Organic Contaminants in the H_2O_2/Periodate Process, Environ. Sci. Technol. 56 (2022) 10372–10380, https://doi.org/10.1021/acs.est.2c02446.

[50] Z. Deng, X.H. Zhang, K.C. Chan, L. Liu, T. Li, Fe-based metallic glass catalyst with nanoporous surface for azo dye degradation, Chemosphere 174 (2017) 76–81, https://doi.org/10.1016/j.chemosphere.2017.01.094.

[51] C. Zhou, Z. Zeng, X. Yu, Y. Li, H. Wei, Q. Zhao, X. Chen, H. Zhang, Enhanced degradation of tetracycline by oxygen-doped porous rod-shaped g-C_3N_4/FeOOH photocatalysts in visible light-driven photocatalytic coupled photo-Fenton system, J. Alloy. Compd. 1064 (2026) 187672, https://doi.org/10.1016/j.jallcom.2026.187672.

[52] L.S. Zhang, X.H. Jiang, Z.A. Zhong, L. Tian, Q. Sun, Y.T. Cui, X. Lu, J.P. Zou, S. L. Luo, Carbon Nitride Supported High-Loading Fe Single-Atom Catalyst for Activation of Peroxymonosulfate to Generate $^1O_2$ with 100% Selectivity, Angew. Chem. Int. Ed. 60 (2021) 21751–21755, https://doi.org/10.1002/anie.202109488.

[53] H. Zeng, Y. Chen, J. Xu, S. Li, J. Wu, D. Li, J. Zhang, Iron-based materials for activation of periodate in water and wastewater treatment processes: The important role of Fe species, Chem. Eng. J. 482 (2024) 148885, https://doi.org/10.1016/j.cej.2024.148885.

[54] R.D. Webster, Electrochemistry combined with electron paramagnetic resonance (EPR) spectroscopy for studying catalytic and energy storage processes, Curr. Opin. Electrochem. 40 (2023) 101308, https://doi.org/10.1016/j.coelec.2023.101308.

[55] Y. Gong, J. Shen, Y. Wu, L. Shen, S. Zhao, Y. Zhou, Y. Li, L. Cui, J. Kang, Z. Chen, Ligands-triggered evolution of catalytic intermediates during periodate activation via soluble Mn(II) for organic contaminants' abatement, Appl. Catal. B-Environ. 322 (2023) 122093, https://doi.org/10.1016/j.apcatb.2022.122093.

[56] H. Sun, F. He, W. Choi, Production of Reactive Oxygen Species by the Reaction of Periodate and Hydroxylamine for Rapid Removal of Organic Pollutants and Waterborne Bacteria, Environ. Sci. Technol. 54 (2020) 6427–6437, https://doi.org/10.1021/acs.est.0c00817.

[57] L. Chen, J. Duan, P. Du, W. Sun, B. Lai, W. Liu, Accurate identification of radicals by in-situ electron paramagnetic resonance in ultraviolet-based homogenous advanced oxidation processes, Water Res. 221 (2022) 118747, https://doi.org/10.1016/j.watres.2022.118747.

[58] A.D. Bokare, W. Choi, Singlet-Oxygen Generation in Alkaline Periodate Solution, Environ. Sci. Technol. 49 (2015) 14392–14400, https://doi.org/10.1021/acs.est.5b04119.

[59] M. Wu, S. Tang, Z. Wang, Q. Zhang, D. Yuan, Molybdenum carbide activated calcium sulfite for antibiotic decontamination at near-neutral pH: Dissolved oxygen promoted bisulfite adsorption for singlet oxygen generation, Chin. Chem. Lett. 36 (2025) 110613, https://doi.org/10.1016/j.cclet.2024.110613.

[60] H. Sun, J. Wang, Y. Jiang, W. Shen, F. Jia, S. Wang, X. Liao, L. Zhang, Rapid aerobic inactivation and facile removal of escherichia coli with amorphous zero-valent iron microspheres: indispensable roles of reactive oxygen species and iron corrosion products, Environ. Sci. Technol. 53 (2019) 3707–3717, https://doi.org/10.1021/acs.est.8b06499.

[61] B. Chakraborty, G. Gan-Or, M. Raula, E. Gadot, I.A. Weinstock, Design of an inherently-stable water oxidation catalyst, Nat. Commun. 9 (2018) 4896, https://doi.org/10.1038/s41467-018-07281-z.